

Biomass burning aerosol transport from Indo-China Peninsula to South China: fluorescence lidar observation and analysis

Zhekai Li^{1,2}, Dawei Tang³, Tianwen Wei^{1,2}, Saifen Yu^{1,2}, Jing Cai^{1,2}, Kenan Wu⁴, Zhen Zhang^{1,2}, Jiadong Hu^{1,2,5}, Haobin Han^{1,2,5}, Yubin Wang^{1,2,5}, and Haiyun Xia^{1,2,5,6}

¹State Key Laboratory of Climate System Prediction and Risk Management, NUIST, Nanjing 210044, China

²School of Atmospheric Physics, NUIST, Nanjing 210044, China

³Academy of Chips Technology, China Electronics Technology Group Corporation, Chongqing 401332, China

⁴School of Information Engineering, Huangshan University, Huangshan 245041, China

⁵Institute of Lidar Technology, GuangZai Co., Ltd., Hangzhou 310005, China

⁶School of Earth and Space Science, University of Science and Technology of China, Hefei 230026, China

Correspondence: Tianwen Wei (twwei@nuist.edu.cn) and Haiyun Xia (hsia@ustc.edu.cn)

Abstract. South China, a densely populated region frequently affected by transported biomass burning aerosol (BBA), requires sensitive remote sensing observations to characterize these plumes. Laser-induced fluorescence (LIF) lidar is a powerful tool for detecting fluorescent aerosol and has recently been demonstrated effective in identifying transported BBA over Europe, while its applications in South China remain scarce. Here, we present LIF lidar observations of fluorescent aerosol conducted at Nanping, South China. The detected fluorescent layer was relatively weak, with a fluorescence signal intensity more than two orders of magnitude lower than the $\text{N}_2\text{-N}_2$ Raman signal intensity (maximum spectral fluorescence backscatter coefficient $\approx 0.16 \times 10^{-5} \text{Mm}^{-1} \text{sr}^{-1} \text{nm}^{-1} \approx 0.16 \times 10^{-5} \text{Mm}^{-1} \text{sr}^{-1} \text{nm}^{-1}$). Nevertheless, it showed a distinct spectral signature compared with typical urban aerosol. Integration of multi-source datasets suggests that the long-range transported BBA emitted by weak fire activity in the Indo-China Peninsula (ICP) was a major contributor to the fluorescent layer. Furthermore, the concurrent presence of BBA and enhanced water vapor indicated a humid environment favorable for aerosol processing. Consistent with the high sensitivity of LIF lidar reported in previous studies, our observations show that weak, long-range transported BBA from the ICP can be observed over South China during periods of relatively weak fire activity, thereby offering new insights into their transport mechanisms and potential environmental impacts.

1 Introduction

Biomass burning aerosol (BBA), predominantly emitted from wildfires, has significant impacts on atmospheric processes and public health. BBA can warm the atmospheric layer in which they reside and play an important role in aerosol–cloud–precipitation interactions (Lin et al., 2014). Once emitted, they undergo complex chemical transformations during transport, which affect downwind air quality and atmospheric composition (Zhou et al., 2017). Among BBA components, biomass burning organic aerosol are of particular concern due to their persistence in the atmosphere and potential health risks (Majdi et al., 2019; Vasilakopoulou et al., 2023). Interactions between wildfires, smoke, and meteorological conditions can also form positive feedback loops that aggravate regional air pollution and associated health outcomes (Huang et al., 2023).

Indo-China Peninsula (ICP), a sub-region of Southeast Asia, is one of the major source regions of BBA in Asia during the pre-monsoon dry season and has substantial impacts on regional air quality and global climate (Yadav et al., 2017). Several international campaigns have investigated BBA in this region, including BASE-ASIA (Biomass-burning Aerosols in South-East Asia: Smoke Impact Assessment) and 7-SEAS (7-South-East Asian Studies) (Lin et al., 2013). Multiple studies have reported that meteorological conditions during the dry pre-monsoon months, particularly March and April, are conducive to vertical lifting of BBA over the ICP. These elevated plumes are subsequently transported eastward under the influence of prevailing monsoonal winds, reaching South China and even the Western Pacific, where they can produce severe health effects. (Chi et al., 2010; Chang et al., 2013; Heese et al., 2017; Nguyen et al., 2020; Qin et al., 2024; Xue et al., 2025; Liu et al., 2025). Therefore, sensitive remote sensing observations are needed in these downwind regions.

As a well-established remote sensing technique, Raman lidar has been widely applied to atmospheric studies (Mattis et al., 2002; Reichardt et al., 2012; Baumgarten, 2010), and has also been adapted for aquatic environments (Shangguan et al., 2023b). Vibrational Raman channels detect molecular scattering and are commonly used as a molecular reference in lidar measurements (Fiedler and Baumgarten, 2024). In early 2005, Immler et al. reported an unexpected enhancement in the water vapor Raman channel signal, which they attributed to fluorescence interference from BBA (Immler et al., 2005). Since then, researchers have developed single-channel (Rao et al., 2018; Li et al., 2019; Veselovskii et al., 2020, 2021; Zhang et al., 2021; Hu et al., 2022; Veselovskii et al., 2022a, b; Jiang et al., 2024; Gast et al., 2025; Yufeng et al., 2025) and multi-channel (~~Sugimoto et al., 2012; Reichardt, 2014; Saito et al., 2018; Reichardt, Jens et al., 2018; Richardson et al., 2019; Reichardt et al., 2023; Wang et al., 2023; Veselovskii et al., 2023, 2024; Huang et al., 2025; Tang et al., 2025a; Veselovskii et al., 2025; Reichardt et al., 2025~~) (Sugimoto et al., 2012; Reichardt, 2014; Saito et al., 2018; Reichardt, Jens et al., 2018; Richardson et al., 2019; Liu et al., 2022; Reichardt et al., 2023; Wang et al., 2023; Veselovskii et al., 2023, 2024; Huang et al., 2025; Tang et al., 2025a; Veselovskii et al., 2025; Reichardt et al., 2025) laser-induced fluorescence (LIF) lidar systems. In addition to observations of the ambient atmosphere, LIF lidar has also been used in the remote sensing of released bioaerosols (Christesen et al., 1993; Simard et al., 2004; Farsund et al., 2012; Wojtanowski et al., 2015; Duschek et al., 2017; Shoshanim, 2023), aquatic oil spills (Leifer et al., 2012; Sun et al., 2023), and chlorophyll (Saito et al., 2016; Zhao et al., 2023; Shangguan et al., 2023a, 2024), highlighting its broad environmental applicability. Previous LIF lidar observations of BBA in the ambient atmosphere, generally built upon Mie-Raman lidar systems, have been conducted mainly in Europe (Reichardt, 2014; Reichardt, Jens et al., 2018; Veselovskii et al., 2020, 2022a, b; Hu et al., 2022; Veselovskii et al., 2023; Reichardt et al., 2023; Veselovskii et al., 2024, 2025; Gast et al., 2025; Reichardt et al., 2025) and have shown that these systems provide high detection sensitivity (Gast et al., 2025; Reichardt et al., 2025). Within these European observations, distinct fluorescent layers and characteristic BBA spectra have been reported, and these layers often originated from long-range transport of BBA from strong fires in North America or Russia. However, BBA fluorescence spectra can vary substantially across locations and cases (Reichardt et al., 2025). Consequently, further observations in diverse regions and under weak fire conditions are warranted, particularly in areas with high biomass burning emission potential and population density such as the ICP and South China, where LIF remote sensing observations remain limited.

Building on these advances, we conducted LIF lidar observations at Nanping, South China, during April–May 2024. Section 2 describes the LIF lidar configuration and the multi-source datasets used in this study. Section 3 describes the calibration and the retrieval of aerosol extinction as well as fluorescence backscatter coefficients from the LIF lidar data. ~~Time-height profiles and fluorescence spectra are presented in Sect.~~ Section 4 reports the observational results: Section 4.1 ~~and 4.2 respectively,~~ revealing first shows the time-height profiles, revealing the presence of a distinct fluorescent layer. ~~Although the overall fluorescence intensity is relatively weak, its spectral signatures differ from those of urban aerosol. To further investigate the origin of this layer,~~ Section 4.2 then investigates its origin using HYSPLIT backward trajectory analysis ~~is presented in Sect. 4.3, demonstrating that the layer originates,~~ indicating that the air mass associated with the fluorescent layer originated from fire sources in the ~~Indo-China Peninsula (ICP). Section~~ ICP. In Sect. 4.3, the fluorescence capacity of the observed layer is quantified based on an assumed lidar ratio, providing a metric to characterize its fluorescence properties. Section 4.4 further analyzes the fluorescence spectra to examine its spectral features. Section 5 ~~compares the~~ provides a comprehensive discussion by integrating the results from Sect. 4. The observed fluorescence characteristics are then compared with previous LIF lidar studies. Additional radiosonde data along the transport pathway are further incorporated in this section. ~~By jointly analyzing radiosonde and LIF lidar data, we find that the BBA layer was transported alongside elevated water vapor, indicating a humid transport pathway.~~ Conclusions and future implications are summarized in Sect. 6.

2 Observations and data

2.1 Multi-channel LIF lidar

The LIF lidar was installed on the top floor of the National Center of Carbon Metrology Building in Nanping City, Fujian Province, China (26.59° N, 118.27° E). ~~The Nanping is a mountainous city in southeastern China characterized by extensive forest coverage and limited heavy industrial activity. Local anthropogenic emissions mainly arise from traffic and residential activities, which may emit combustion-related organic aerosols. In addition, the surrounding vegetated environment associated with the region's high forest coverage may release primary biological aerosol particles. The lidar system emitted a 355 nm laser beam from an Nd:YAG laser (Innolas Spotlight EVOIII) with pulse energy exceeding 200 mJ. The laser beam was then expanded by a 10 × beam expander and subsequently directed into the atmosphere at an elevation angle of 30° via a reflector.~~ The vertical altitude was obtained by projecting the slant range onto the vertical direction, and all altitudes reported hereafter refer to vertical altitude. The backscattered signal was gathered by a 12-inch telescope (Meade LX 200) and detected by the lidar detector equipped with a 32-channel photomultiplier tube (Licel SP32HR). A 355 nm optical notch filter was placed between the telescope and the detector to suppress elastic signal leakage. Many types of atmospheric aerosol can produce fluorescence under UV laser excitation, particularly organic carbon (OC), a major component of BBA. The dominant fluorescence emission wavelength is observed within 400–650 nm when excited by a 351 nm laser (Pan, 2015). To simultaneously capture both Raman and fluorescence signals (~~Table 1~~), the spectrometer central wavelength was set to 475 nm in this study, with a spectral resolution of ~~6.2 nm nm⁻¹~~ 6.2 nm nm⁻¹. Accordingly, the effective detection ranges of the 32 channels (Channels 31–0) cover central wavelengths from 378.9 to 571.1 nm. ~~All detection channels are listed in Table 1. The vibrational overtone of N₂~~

Raman scattering at 424.4 nm (Veselovskii et al., 2023) falls within the spectral range of Channel 24, leading to minor spectral features in this channel (as shown in Fig. 1). Four observation cases (Cases 1–4) in April and May 2024 were discussed. A distinct fluorescent layer was identified in Case 1, while the remaining cases were analyzed for comparison. Further technical details of the LIF lidar system can be found in (Tang et al., 2025a).

Table 1. Spectral channel configuration of the LIF lidar. Channel indices decrease with increasing wavelength.

Detection signal	Central wavelength (nm)	Channel index
N ₂ Raman	385.1	30
H ₂ O Raman	403.7	27
N ₂ Overtone	422.3	24
Fluorescence	434.7–571.1	22–0

2.2 Satellite, radiosonde and ground-based observations

The Moderate-Resolution Imaging Spectroradiometer (MODIS) is a spaceborne multispectral sensor widely used in BBA studies (Shi et al., 2019; Yin, 2020). In this study, we utilized the MODIS Corrected Reflectance (True Color) imagery acquired on 16 April 2024, to visually overview fire activities in the ICP. We selected two sub-regions from the imagery to illustrate the spatial distribution of fire sources (Fig. 54a–b). To further quantify and identify fire events, we obtained the MODIS Collection 6.1 (C6.1) standard active fire product from NASA’s Fire Information for Resource Management System (FIRMS) (Giglio et al., 2016). This dataset includes fire locations, fire radiative power (FRP), detection confidence, and fire types. For quality control, we used fire points that had confidence > 80 %, FRP > 100 MW, and were classified as type 0 (presumed vegetation fires).

To get the water vapor mixing ratio (WVMR) profiles, we used radiosonde data of five cities in South China downloaded from the University of Wyoming’s website (<https://weather.uwyo.edu/>); the location distributions are shown in Fig. 7a. To avoid cloud contamination in the radiosonde profiles, we discarded any level with relative humidity (RH) exceeding 95 %, following the approach of Zhou et al. (2025).

The AERosol ROBOTIC NETwork (AERONET) (Holben et al., 1998) is a global ground-based aerosol monitoring program jointly established by NASA and PHOTONS (a European initiative coordinated by the University of Lille, the French National Centre for Space Studies, and the National Institute for Earth Sciences and Astronomy of CNRS). To support the identification of BBA transport events, we selected three AERONET sites near burning areas in the ICP (Chiang_Mai_Met_Sta, Doi_Ang_Khang, and Luang_Namtha); their geographic locations are marked as red triangles in Fig. 54e. Temporal variations in the aerosol optical depth at 500 nm (AOD@500 nm) provided auxiliary evidence for biomass burning plumes. We obtained air pollution data (including ~~PM_{2.5} and PM₁₀~~ PM_{2.5} and PM₁₀ concentrations) from the China National Environmental Mon-

itoring Centre (CNEMC). To reduce localized variability and measurement noise, we averaged data from three monitoring stations near the LIF lidar site.

115 2.3 Reanalysis data and trajectory model

ERA5 (Hersbach et al., 2020) is the fifth-generation global climate reanalysis dataset from the European Centre for Medium-Range Weather Forecasts (ECMWF). In this study, we used ERA5 data to characterize temperature, geopotential, wind fields, and RH at different altitudes, providing essential meteorological context for our analysis. The Modern-Era Retrospective analysis for Research and Applications, Version 2 (MERRA-2) is a long-term global reanalysis developed by NASA's Global
120 Modeling and Assimilation Office (GMAO). It assimilates satellite-based aerosol observations to represent interactions between aerosols and other physical processes in the climate system (Gelaro et al., 2017). In this study, we used hourly biomass burning OC emissions from the MERRA-2 `tavg1_2d_adg_Nx` hourly dataset with a spatial resolution of $0.625^\circ \times 0.5^\circ$.

The Hybrid Single-Particle Lagrangian Integrated Trajectory (HYSPLIT) model, developed by NOAA's Air Resources Laboratory, is widely used to analyze atmospheric transport, dispersion, air parcel trajectories, and pollutant transport pathways
125 (Stein et al., 2015). In this study, we employed 78-hour backward trajectory analysis using the HYSPLIT model, initialized at the LIF lidar site, aiming to identify the transport history and potential source regions of the observed fluorescent aerosol layer. The meteorological inputs were from the Global Data Assimilation System (GDAS).

3 LIF lidar data processing

3.1 Ghost line calibration

130 The calibration procedure was initially performed on the original fluorescence spectrum. Additionally, unavoidable imperfections in the diffraction grating can cause periodic spectral artifacts in fluorescence spectra, especially under weak fluorescence conditions. In our study, minor spurious peaks were found at Channels 21, 16, and 10 (Fig. 1). These peaks, known as Lyman ghosts (Tang et al., 2025a), were corrected based on their dependence on the primary wavelength (N_{2-2} Raman signal; Channel 30, with a central wavelength of 385.1 nm) (Meggers and Kiess, 1922). In Fig. 1, the spectra are normalized by the N_{2-2} Raman
135 signal. For each case, both uncorrected and corrected curves are shown for direct comparison. To quantify ghost contributions and standardize correction across all spectral data, we selected three spectra with the lowest fluorescence intensity from three cases (where the N_{2-2} Raman signal maintains sufficient intensity to ensure calibration reliability). One of them is the spectrum from Case 4 (2.0–2.8 km), which is shown in Fig. 1. For this spectrum, the three ghost-affected intervals (Channels 21, 16, and
140 10) were removed and reconstructed using linear interpolation, yielding a ghost-free reference spectrum (bottom blue dashed line in Fig. 1). The differences between the two blue curves at the three affected channels represent the characteristic ghost contribution for each channel. Ghost correction coefficients were then defined as these channel-specific differences divided by the corresponding N_{2-2} Raman signal intensity from the same spectrum. The final channel-specific ghost correction coefficients were obtained by averaging the corresponding coefficients from the three reference spectra. All analyzed spectra were

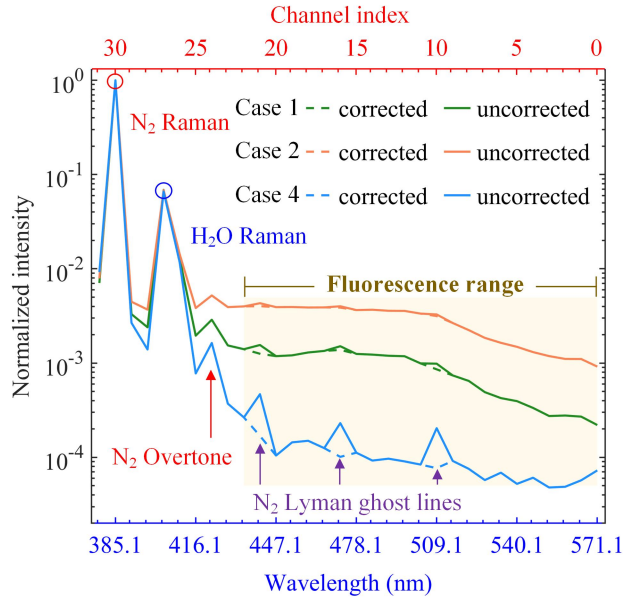


Figure 1. Mean fluorescence spectra for Cases 1 (1.0–1.8 km), 2 (1.0–1.8 km), and 4 (2.0–2.8 km) measured at the LIF lidar site. Line colors indicate the different cases. Solid lines show spectra before ghost-line correction and dashed lines show spectra after ghost-line correction (see legend). All the spectra are normalized by the N_{2-2} Raman signal.

corrected using the same three coefficients (one per ghost-affected channel). During the correction, ghost contributions were estimated as the product of the N_{2-2} Raman signal intensity and channel-specific coefficients, and subsequently subtracted from the original values to obtain the corrected spectra. Representative results for Cases 1 and 2 are shown in Fig. 1, where the dashed lines denote ghost-free spectra.

3.2 Retrieval of aerosol extinction and fluorescence backscatter coefficients

The aerosol extinction coefficient at distance z from the lidar is given by (Ansmann et al., 1990):

$$D = d/dz \left\{ \ln \left[N_R(z) / P_R(z) z^2 \right] \right\} \quad (1)$$

$$\alpha_L^{\text{aero}}(z) = \frac{D - \alpha_L^{\text{mole}}(z) - \alpha_R^{\text{mole}}(z)}{1 + (\lambda_L/\lambda_R)^k} \quad (2)$$

where the superscripts "aero" and "mole" indicate quantities related to aerosols and molecules, respectively. The subscripts "L" and "R" correspond to elastic and N_{2-2} Raman channels. α_R^{mole} and α_L^{mole} are the molecular extinction coefficients in elastic and N_2 Raman channels, calculated following (Platt et al., 2012). N_R is the nitrogen concentration-profile number density, which is calculated using the standard atmosphere model (Shang et al., 2018) from temperature and pressure values obtained from the

ERA5 reanalysis dataset. λ_L and λ_R denote the elastic wavelength (~~355 nm~~) and the N_2 Raman channel central wavelength (385.1 nm), respectively. The Ångström exponent k is assumed to be 1 (Ansmann et al., 1992a).

The fluorescence backscatter coefficient is given by (Veselovskii et al., 2020):

$$\beta_F = \frac{C_R}{C_F} \frac{P_F}{P_R} \frac{T_R}{T_F} N_R \sigma_R \quad (3)$$

160 where ~~P_F and P_R~~ and P_F are the lidar signals from the ~~fluorescence and N_2 Raman~~ N_2 Raman and fluorescence (Channels 22–0, with central wavelengths of 434.7–571.1 nm) channels, respectively. σ_R is the N_2 Raman differential backscatter cross section at 355 nm (Venable et al., 2011). T_R and T_F are the atmospheric transmittance for the N_2 Raman and fluorescence (~~Channels 22–0, with central wavelengths of 434.7–571.1 nm~~) channels, respectively. C_R and C_F are system constants for the N_2 Raman and fluorescence channels, respectively. Similarly, the water vapor Raman backscatter coefficient ~~β_{H_2O}~~ β_{H_2O} is derived
165 by replacing the fluorescence channels with the water vapor Raman channel (~~channel~~ Channel 27, with a central wavelength of 403.7 nm). Unlike single-channel fluorescence systems, our LIF lidar employs 23 fluorescence channels. Accordingly, the fluorescence backscatter coefficient β_F is obtained by summing contributions from all individual channels. For comparison, β_F is then normalized by the fluorescence spectral wavelength range $\Delta\lambda$ to yield the spectral fluorescence backscatter coefficient:

$$\bar{\beta}_F = \frac{\beta_F}{\Delta\lambda} \quad (4)$$

170 4 Results

4.1 Vertical profiles observed by LIF lidar

Time-height profiles of four representative nighttime cases observed in 2024 are shown in Fig. 2. All observations were conducted at night to avoid strong solar background interference during the daytime. Four cases are included: Case 1 (19 April, 23:19–20 April, 00:05), when a distinct fluorescence layer was observed (Fig. 2c); Case 2 (11 May, 01:41–02:37); Case 3 (18
175 May, 21:43–23:29); and Case 4 (23 May, 21:27–23:08). All times are in local time (UTC+8), with the time axis labeled at 20 minute intervals. The vertical white lines separate individual cases. Figure 2a–c show the range-corrected signal (RCS) of different detection channels, while Fig. 2d–f present retrieved parameters derived via the methods described in Sect. 3.2. ~~Due to the LIF lidar’s 30° elevation angle, the effective detection height equals half of the line-of-sight range.~~ The detection lower limit is within 800 m, which defines the starting altitude of all subplots. The N_2 Raman signal (Fig. 2a) decays more slowly in
180 Case 4 than in the other three cases, likely due to the lower aerosol loading (Fig. 2d and Fig. A1a). The fluorescence intensity is also relatively weak in Case 4 (Fig. 2c, f, and Fig. 3), making this case ideal for calibrating the Lyman ghost lines. In Cases 1, 3, and 4 (3–4 km), we observed abrupt enhancements in $\alpha_L^{\text{aero}}(z)$ (Fig. 2d), indicating the presence of clouds (Sugimoto et al., 2012). In Case 3, the fluorescence layer ascends to ~3 km due to the vertical mixing (Fig. 2f). This upward shift is further evident in Fig. 3, where the averaged $\bar{\beta}_F$ (0.8–1.4 km) decays rapidly in all cases except Case 3.

185 Figure A1 presents the relationships among averaged $\bar{\beta}_F$, α_L^{aero} (0.8–1.4 km), surface RH, and surface PM concentrations. In Cases 1 and 4, RH remains close to saturation following preceding precipitation, favoring efficient wet deposition and resulting

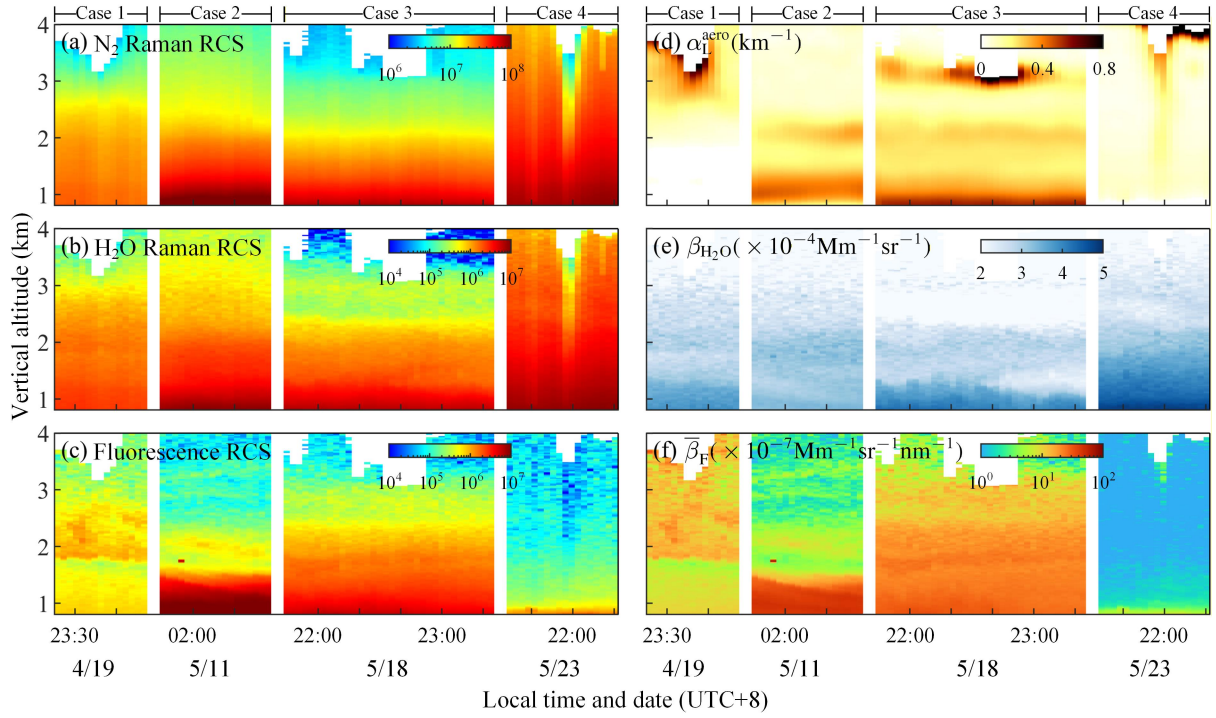


Figure 2. Time-height profiles for the four cases at the LIF lidar site during 19 April–23 May 2024 (UTC+8). (a–c) The range-corrected signal (RCS) from the respective detection channels (as defined in Table 1). (d–f) Retrieved quantities for (a–c), respectively; retrieval methods are described in Sect. 3.2.

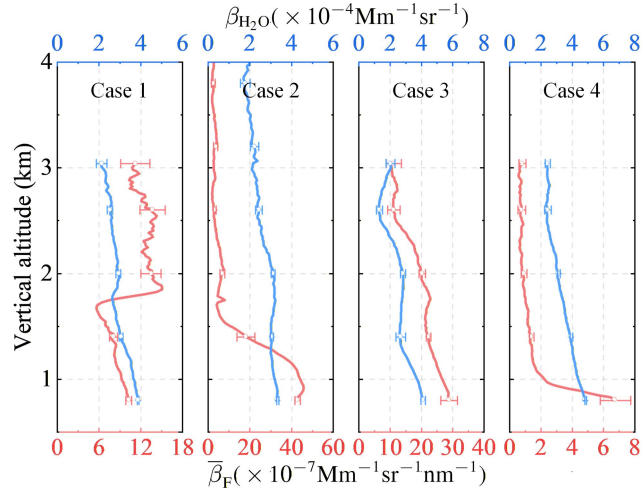


Figure 3. Mean vertical profiles of $\beta_{\text{H}_2\text{O}}$ (blue lines) and $\bar{\beta}_{\text{F}}$ (red lines) for the four cases at the LIF lidar site. Error bars indicate ± 1 standard deviation across the profile samples.

in reduced aerosol loading. Consequently, lower α_L^{aero} ($< 0.05 \text{ km}^{-1}$ – 0.1 km^{-1}) are observed compared to Cases 2 and 3 ($> 0.15 \text{ km}^{-1}$ – 0.3 km^{-1}), which qualitatively agrees with the observed PM concentration differences. The slightly negative layer-averaged α_L^{aero} in Case 1 can be attributed to retrieval uncertainties under very clean conditions, a behavior also reported in
190 previous studies (Ansmann et al., 1992b; Hu et al., 2025). In particular, hygroscopic growth under elevated RH can enhance aerosol optical extinction by modifying particle size and refractive index (Ansmann et al., 1992a; Haarig et al., 2025). This effect likely contributes to the slightly higher α_L^{aero} in Case 2 compared to Case 3 (RH $\approx 89.2\%$ –~~versus~~ $\approx 83.6\%$ $\approx 89.2\%$ ~~versus~~ $\approx 83.6\%$). In contrast to aerosol extinction, fluorescence signals are expected to be much less affected by ambient humidity and hygroscopic growth. Under the assumption of minimal water-induced fluorescence quenching (Veselovskii et al.,
195 2025a), negligible hygroscopic effects on aerosol fluorescence, and unchanged aerosol mixing state, $\bar{\beta}_F$ can be regarded as a reliable proxy for dry aerosol material concentrations (Miri et al., 2024), which is consistent with the dry-state nature of the measured PM mass concentrations. However, the relative magnitudes of $\bar{\beta}_F$ in Cases 2 and 3 still exhibit an opposite ordering compared to PM concentrations, indicating that aerosol fluorescence does not scale linearly with bulk particulate mass. This discrepancy reflects the combined influence of fluorescent particle types and concentrations, rather than particle mass alone
200 (Reichardt, 2014).

In Case 1, a distinct fluorescent layer (enhanced $\bar{\beta}_F$) accompanied by enhanced water vapor was observed at ~ 1.8 – 1.8 km despite relatively low α_L^{aero} (Fig. 2c, e, f, and Fig. 3). This enhancement is not observed in the other three cases (Fig. 3). To better constrain the aerosol source in Case 1 (1.8–2.4 km), HYSPLIT backward trajectory analysis was performed in Sect. 4.2.

205 4.2 Source attribution of the fluorescent layer in Case 1

HYSPLIT backward trajectories for Case 1 indicate that the air mass linked to the fluorescent layer originated from the ICP during 16–18 April 2024 (Fig. 4d). This event can be divided into three stages: local biomass burning, vertical lifting, and long-range transport. MODIS true-color imagery for 16–17 April (Fig. 4a–b) reveals multiple fire points, with near-surface plume orientations consistent with winds blowing toward the northeast (Fig. 4f–g). Two source regions with the most intense
210 fire activity are highlighted by black boxes in Fig. 4d–g (these boxes correspond to the areas as in Fig. 4a–b). MODIS C6.1 fire products also identify numerous low-intensity vegetation fire pixels within these regions (Fig. 4d), while the MERRA-2 emission fields indicate elevated OC emissions coincident with these suspected sources (Fig. 4f–g). Additionally, the 10-m wind barbs align with the plume directions visible in the satellite imagery. As shown in Fig. 5, AOD@500 nm at three AERONET stations (locations marked as red triangles in Fig. 4e) increased during the period. The BBA then underwent vertical lifting to
215 the 2–3 km altitude range (Fig. 4c). During the pre-monsoon season, frequent small-scale cumulus convection can transport pollutants above 3 km—an optimal altitude for long-range transport (Shan et al., 2016). For our case, a similar phenomenon was visible in Fig. 4a–b. Additionally, the higher terrain (Fig. 4d) also provides favorable conditions for BBA uplift. Thereafter, the BBA were rapidly transported by the southwest summer monsoon (Fig. 4d) to altitudes above our LIF lidar site, where a fluorescent layer was observed. On the contrary, HYSPLIT backward trajectory analysis with a starting altitude of 1 km show
220 that the low-altitude fluorescence was not affected by the transported BBA (Fig. B1).

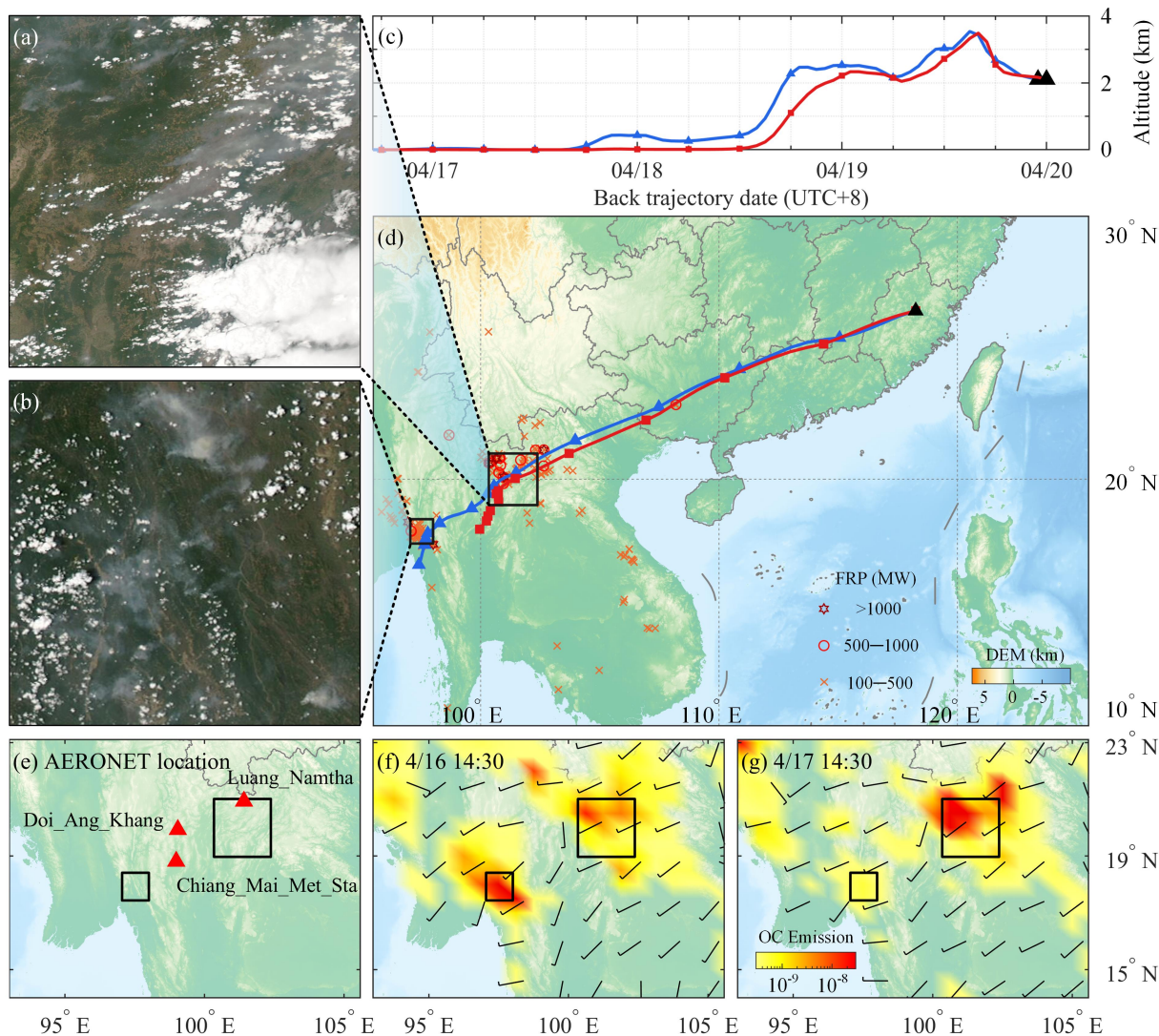


Figure 4. Imagery, trajectory analysis and modeled biomass burning emissions for Case 1. (a–b) MODIS (Aqua) true-color images acquired on 16 April 2024 (UTC), sourced from NASA Worldview (<https://worldview.earthdata.nasa.gov/>), showing smoke plumes originating from multiple fire points (areas highlighted by black boxes in panels d–g). (c) Vertical variation of air mass altitude from HYSPLIT backward trajectories (starting altitude: 2.1 km). (d) Horizontal (longitude-latitude) HYSPLIT backward trajectories overlaid on presumed vegetation fire locations; marker colors and shapes indicate FRP levels, and the underlying digital elevation model (DEM) highlights topography (the black triangle denotes the LIF lidar site). (e) Locations of the AERONET stations (red triangles) used in Fig. 5. (f–g) MERRA-2 biomass burning organic carbon (OC) emissions ($\text{Kg m}^{-2} \text{s}^{-1}$) for two temporal conditions, plotted with background 10-m wind fields.

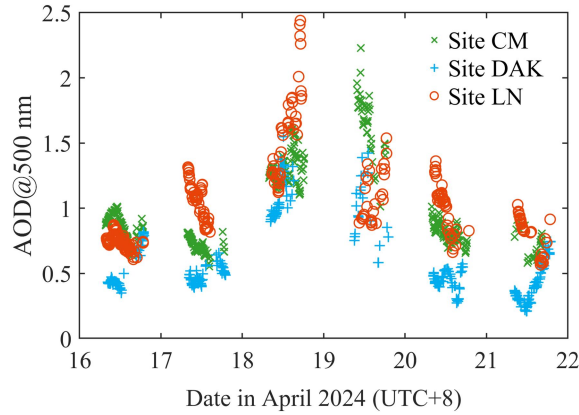


Figure 5. Aerosol optical depth at 500 nm (AOD@500 nm) retrieved from three AERONET sites during 16–22 April 2024. Marker colors and shapes indicate the stations: CM represents Chiang_Mai_Met_Sta, DAK represents Doi_Ang_Khang, and LN represents Luang_Namtha (locations shown in Fig. 4e, red triangles).

4.3 Spectral fluorescence capacity estimation

To further analyze the fluorescence characterization, we use quantitative analyses of the spectral fluorescence capacity $G_F = \frac{\bar{\beta}_F}{\beta_L}$, where $\bar{\beta}_F$ is the spectral fluorescence backscatter coefficient and β_L is the elastic backscatter coefficient (Reichardt, 2014; Veselovskii et al., 2022b). As β_L was not directly available in this study, we estimated $\hat{G}_F = \frac{\bar{\beta}_F}{\alpha_L^{\text{aero}}} \cdot S$ using a typical lidar ratio $S \approx 55$ sr for aged smoke (Ansmann et al., 2021). To enable direct comparability with the fluorescence wavelength range (444–488 nm) from (Gast et al., 2025), we selected Channels 20–14 (444–487.4 nm) for \hat{G}_F estimation. \hat{G}_F values are provided in Table 2, excluding Case 1 (0.8–1.4 nm): negative α_L^{aero} results in negative \hat{G}_F , which is thus omitted. Table 2 presents the highest \hat{G}_F for Case 1 (1.8–2.4 km) $\approx 3.1 \times 10^{-6} \text{ nm}^{-1}$, which falls within the typical smoke range of $2 \times 10^{-6} \approx 1.6 \times 10^{-6} \text{ nm}^{-1}$, which is close to the lower bound of the G_F range ($1.5 \times 10^{-6} - 9 \times 10^{-6} \text{ nm}^{-1}$) (Gast et al., 2025) and $13 \times 10^{-6} \text{ nm}^{-1}$) reported for smoke observed in Germany (Gast et al., 2025). Notably, \hat{G}_F for Case 1 (1.8–2.4 km) is at least twice as high as \hat{G}_F values from other layers those retrieved from the other layers, indicating relatively enhanced fluorescence efficiency in this layer. The characteristics of the fluorescent layer are further examined through analysis of the fluorescence spectra in Sect. 4.4.

4.4 Fluorescence spectra

As shown in Fig. 46a, mean fluorescence spectra from multiple 600 m thick layers are normalized to the N_{2-2} Raman signal. The maximum fluorescence intensity is more than two orders of magnitude lower than that of the N_{2-2} Raman signal. To quantitatively analyze the spectral similarity, we adopted the spectral angle mapping (SAM) analysis (Farsund et al., 2010) using Channels 20–14 (444–487.4 nm) from the fluorescence spectra. This algorithm quantifies spectral similarity by treating spectra as vectors and calculating the vector angle, ranging from 0° (identical spectral shapes) to 90° (completely distinct

Table 2. Estimates of layer-averaged spectral fluorescence capacity ($\hat{G}_F = \frac{\bar{\beta}_F}{\alpha_{L,aero}^L} \cdot S$), computed over the fluorescence spectral range 444–487.4 nm (Channels 20–14). A lidar ratio S of 55 sr (typical for aged smoke) is assumed (Ansmann et al., 2021).

Cases	\hat{G}_F ($\times 10^{-6} \text{ nm}^{-1} \times 10^{-6} \text{ nm}^{-1}$) (0.8–1.4 km)	\hat{G}_F ($\times 10^{-6} \text{ nm}^{-1} \times 10^{-6} \text{ nm}^{-1}$) (1.8–2.4 km)
Case 1	—	3.1–1.6
Case 2	1.5–0.7	0.4–0.2
Case 3	1.2–0.6	1.4–0.6
Case 4	0.5–0.3	0.2–0.1

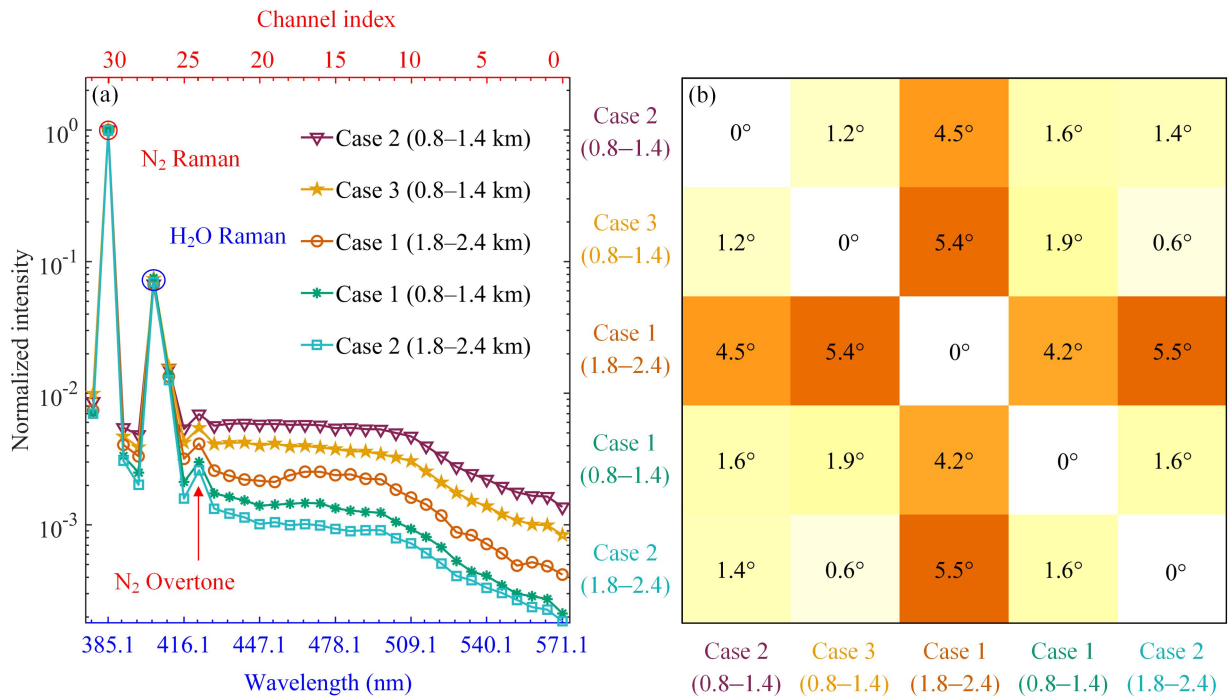


Figure 6. (a) Mean fluorescence spectra (normalized by N_2 Raman signal) derived from 600 m-thick layers for Cases 1–3. Line colors and marker shapes denote the different cases and layer altitudes (see legend). (b) SAM angle matrix for the five selected spectra (Channels 20–14, 444–487.4 nm). A SAM angle of 0° indicates identical spectral shapes, with larger angles corresponding to greater dissimilarity.

240 spectral shapes). Fig. 46b shows the SAM angle matrix for the selected spectra in Fig. 46a. The low SAM angle ($\approx 1.14^\circ \approx 1.2^\circ$) between Cases 2 and 3 (0.8–1.4 km) indicates high spectral similarity. Both spectra exhibit decreasing intensity with increasing wavelength, consistent with reported urban aerosol spectra in the boundary layer (Veselovskii et al., 2025). **Considering these**

spectral features with the low \hat{G}_F ($\leq 1.5 \times 10^{-6} \text{ nm}^{-1}$; Table 2) and the higher averaged α_L^{aero} (0.8–1.4 km) in Cases 2 and 3 compared to Cases 1 and 4 (linked with PM concentration trends; Fig. A1), our results suggest that the fluorescence of Cases 2 and 3 (0.8–1.4 km) observed at our LIF lidar site was likely attributable to urban aerosol. Regarding potential biogenic interference, although local dominant tree species (e.g., pines) may release pollen in May, pollen is unlikely to be the dominant contributor to the fluorescence signal in Cases 2 and 3 (0.8–1.4 km). This is evidenced by the absence of distinct characteristic peaks in the fluorescence spectra (Saito et al., 2018) and the low \hat{G}_F .

The spectrum of Case 1 (1.8–2.4 km) is distinct from other spectra (Fig. 46a), with quantitative support from spectral angle mapping (SAM) analysis (Fig. 46b): the SAM angle between Case 1 (1.8–2.4 km) and Cases 2 and 3 (0.8–1.4 km; urban aerosol) is $\sim 4.9^\circ$ is $\sim 5.0^\circ$, notably larger than the SAM angle ($\approx 1.14^\circ \approx 1.2^\circ$) between Cases 2 and 3 (0.8–1.4 km) themselves. Additionally, SAM angles between Case 1 (1.8–2.4 km) and Case 1 (0.8–1.4 km) as well as between Case 1 (1.8–2.4 km) and Case 2 (0.8–1.8–2.4 km) both exceed 4° , further confirming the spectral dissimilarity. To better constrain the aerosol source in Case 1 (1.8–2.4 km

255 5 Discussion

Considering the distinct $\bar{\beta}_F$ layer (Fig 2f), HYSPLIT backward trajectory analysis was performed in Sect. 4.3.

Imagery, trajectory analysis and modeled biomass burning emissions for Case 1. (a–b) MODIS (Aqua) true-color images acquired on 16 April 2024 (UTC), sourced from NASA Worldview (<https://worldview.earthdata.nasa.gov/>), showing smoke plumes originating from multiple fire points (areas highlighted by black boxes in panels d–g). (c) Vertical variation of air mass altitude from HYSPLIT backward trajectories (starting altitude: 2.1 km). (d) Horizontal (longitude–latitude) HYSPLIT backward trajectories overlaid on presumed vegetation fire locations; marker colors and shapes indicate FRP levels, and the underlying digital elevation model (DEM) highlights topography (the black triangle denotes the LIF lidar site). (e) Locations of the AERONET stations (red triangles) used in Fig. 6. (f–g) MERRA-2 biomass burning organic carbon (OC) emissions ($\text{Kg m}^{-2} \text{ s}^{-1}$) for two temporal conditions, plotted with background 10-m wind fields.

265 Aerosol optical depth at 500 nm (AOD@500 nm) retrieved from three AERONET sites during 16–22 April 2024. Marker colors and shapes indicate the stations: CM represents Chiang_Mai_Met_Sta, DAK represents Doi_Ang_Khang, and LN represents Luang_Namtha (locations shown in Fig. 5e, red triangles).

HYSPLIT backward trajectories for Case 1 indicate that the air mass linked to the fluorescent layer originated from the ICP during 16–18 April 2024 (Fig. 5d). This event can be divided into three stages: local biomass burning, vertical lifting, and long-range transport. MODIS true-color imagery for 16–17 April (Fig. 54d), the highest \hat{G}_F ($\approx 1.6 \times 10^{-6} \text{ nm}^{-1}$; Table 2) and the unique fluorescence spectral shape (Fig 6a–b) reveals multiple fire points, with near-surface plume orientations consistent with winds blowing toward the northeast (Fig. 5f–g). Two source regions with the most intense fire activity are highlighted by black boxes in Fig. 5d–g (these boxes correspond to the areas as in Fig. 5a–b). MODIS C6.1 fire products also identify numerous low-intensity vegetation fire pixels within these regions (Fig. 5d), while the MERRA-2 emission fields indicate elevated OC emissions coincident with these suspected sources (Fig. 5f–g). Additionally, the 10-m wind barbs align with the

275

plume directions visible in the satellite imagery. As shown in Fig. 6, AOD@500 nm at three AERONET stations (locations marked as red triangles in Fig. 5c) increased during the period. The BBA then underwent vertical lifting to the 2–3 km altitude range (Fig. 5c). During the pre-monsoon season, frequent small-scale cumulus convection can transport pollutants above, these lines of evidence support that BBA transported from the ICP was a major contributor to the fluorescent layer observed in Case 1 (1.8–2.4 km). For the fluorescence spectra of Cases 2 and 3 (0.8–1.4 km), considering the spectral features in Sect. 4.2 with the low \hat{G}_F ($\leq 1 \times 10^{-6} \text{ nm}^{-1}$; Table 2) and the higher averaged α_L^{aero} (0.8–1.4 km) in Cases 2 and 3 km—an optimal altitude for long-range transport (Shan et al., 2016). For our case, a similar phenomenon was visible in Fig. 5a–b. Additionally, the higher terrain (compared to Cases 1 and 4 (linked with PM concentration trends; Fig. 5d) also provides favorable conditions for BBA uplift. Thereafter, the BBA were rapidly transported by the southwest summer monsoon (Fig. 5d) to altitudes above A1), our results suggest that the fluorescence of Cases 2 and 3 (0.8–1.4 km) observed at our LIF lidar site, where a fluorescent layer was observed. Considering the distinct $\bar{\beta}_F$ layer (Fig. 2f), the highest \hat{G}_F ($\approx 3.1 \times 10^{-6} \text{ nm}^{-1}$; Table 2), the unique fluorescence spectral shape (Fig. 4a–b), and HYSPLIT backward trajectory analysis (Fig. 5d), these lines of evidence support that BBA transported from the ICP was a major contributor to urban aerosol. Regarding potential biogenic interference, although local dominant tree species (e.g., pines) may release pollen in May, pollen is unlikely to be the dominant contributor to the fluorescent layer observed in Case 1 (1.8–2.4 km) fluorescence signal in Cases 2 and 3 (0.8–1.4 km). On the contrary, HYSPLIT backward trajectory analysis with a starting altitude of 1 km show that the low-altitude fluorescence was not affected by the transported BBA (Fig. B1). This is evidenced by the absence of distinct characteristic peaks in the fluorescence spectra (Saito et al., 2018) and the low \hat{G}_F .

The Asian summer monsoon brings substantial rainfall to the region, while the pre-monsoon season (March–April) is typically dry across the ICP. During this period, frequent biomass burning events (predominantly forest fires and agricultural burnings) lead to seasonal peaks in BBA loadings (Gautam et al., 2013; Shi and Yamaguchi, 2014). Fire activity peaks in March but declines sharply by late April (Huang et al., 2016). MODIS FRP data indicate that over 84 % of fire points had FRP < 500 MW (with only a few high-intensity points), while MERRA-2 data show a maximum OC emission rate of $1.5 \times 10^{-8} \text{ Kg m}^{-2} \text{ s}^{-1}$. The detected fluorescent layer was relatively weak, with a fluorescence signal intensity more than two orders of magnitude lower than the N_{22} Raman signal intensity. The maximum $\bar{\beta}_F \approx 0.16 \times 10^{-5} \text{ Mm}^{-1} \text{ sr}^{-1} \text{ nm}^{-1}$ observed in Case 1 (1.8–2.4 km) lies at the lower end of the range of $\bar{\beta}_F$ values reported for BBA in France (Hu et al., 2022), Germany (Gast et al., 2025; Reichardt et al., 2025), and Russia (Veselovskii et al., 2025). Consistent with the high sensitivity of LIF lidar reported in previous studies (Gast et al., 2025; Reichardt et al., 2025), our results show that weak, long-range transported BBA from the ICP can be observed over South China during periods of relatively weak fire activity (e.g., late April).

For the spectrum of Case 1 (1.8–2.4 km), the relatively weak peak intensity is likely attributable to the overall low fluorescence signal intensity (which is over two orders of magnitude lower than the N_{22} Raman signal) and mixing with urban aerosol due to the long-range transport, while the peak wavelength discrepancy relative to previous studies is likely due to distinct fire sources. Biomass burning emits complex carbonaceous aerosols, which undergo further chemical transformations during atmospheric transport and result in more diverse compositions (Hodshire et al., 2019; Wang et al., 2019). Many components in

BBA, such as polycyclic aromatic hydrocarbons (PAHs) and humic-like substances (HULIS), can produce fluorescence under UV excitation (Pöhlker et al., 2012; Yue et al., 2022). As shown in Fig. 46a, Case 1 (1.8–2.4 km) exhibited a spectral shoulder which begins at Channel 18 (central wavelength is 459.5 nm), suggesting the presence of fluorophores. As summarized in Table C1, fluorescence peaks in the 440–480 nm range have been reported for certain PAHs and HULIS under ~355 nm excitation, which are similar to our observed spectral feature. In contrast, previous LIF lidar observations in Europe exhibited BBA fluorescence peak wavelengths approximately between 498 and 560 nm (Table C2), highlighting the influence of source characteristics and atmospheric processing on spectral signatures. Via vertical mixing, such transported BBA may influence the near-surface atmosphere (Dajuma et al., 2020). Future observations combining LIF lidar with in-situ instrumentation such as the Wideband Integrated Bioaerosol Sensor (WIBS), which also operates on LIF principles (Tang et al., 2022), would facilitate a more in-depth investigation of the near-surface impacts exerted by transported BBA. Combined LIF lidar and WIBS measurements have recently been reported (Gidarakou et al., 2025)(Gidarakou et al., 2026).

To further investigate BBA transport processes, we analyzed radiosonde observations from multiple sites in South China (Fig. 7a), with colors representing different observation times corresponding to the BBA transport period (Fig. 54d, the "long-range transport" stage). In Fig. 7g, the $\bar{\beta}_F$ shows a marked increase at 1.8 km, coinciding with enhanced β_{H_2O} at Nanping. ~~Although previous studies have noted~~ Previous studies have suggested that fluorescence interference in water vapor Raman channels (Chouza et al., 2022; Liu et al., 2022) may contribute to an enhancement in β_{H_2O} . However, in our measurements, ~~our measurements show~~ the fluorescence signal ~~was roughly an~~ is approximately one order of magnitude lower than the water vapor ~~signal (shown in Raman signal (Fig. 4a), indicating that~~ 6a). As a sensitivity test, we subtracted the signal from a nearby fluorescence channel (Channel 22) from the water vapor Raman channel and found that the enhanced β_{H_2O} layer persists, suggesting that fluorescence interference is ~~unlikely to be the primary cause of the observed~~ β_{H_2O} enhancement. ~~The limited.~~ In addition, the ERA5 RH profile (Fig. 7h) ~~additionally verifies the~~ shows a distinct high-humidity layer at the same altitude, which is consistent with the presence of a ~~high-humidity real moisture~~ layer. As shown in Fig. 54d, HYSPLIT backward trajectories indicate that the observed BBA layer originated from fire sources near coastal regions and was transported inland by onshore flow, which suggests possible entrainment of marine aerosols (such as sea salt) (Dang et al., 2022). Furthermore, radiosonde data (Fig. 7b–f) reveal that the BBA was co-transported with water vapor, a feature consistent with previous lidar and in-situ observations (Kim et al., 2009; Fadnavis et al., 2013; Pistone et al., 2021; Chavan et al., 2021; Hu et al., 2022; Rubin et al., 2023; Pistone et al., 2024). Such humid, sea salt containing conditions could enhance sunlight driven reactions, accelerating secondary sulfate formation and thereby exerting important environmental impacts (Tang et al., 2023, 2025b).

5 Conclusion

In this study, we report LIF lidar observations at Nanping, South China during April–May, 2024. A distinct fluorescent layer was observed, exhibiting unique spectral characteristics and an estimated fluorescence capacity ($\hat{G}_F \approx 3.1 \times 10^{-6} \text{ nm}^{-1}$ $\hat{G}_F \approx 1.6 \times 10^{-6} \text{ nm}^{-1}$). HYSPLIT backward trajectory analysis indicates that this layer originated from low-intensity fire points in the ICP. These lines of evidence support that the BBA transported from the ICP was a major contributor to the fluorescent

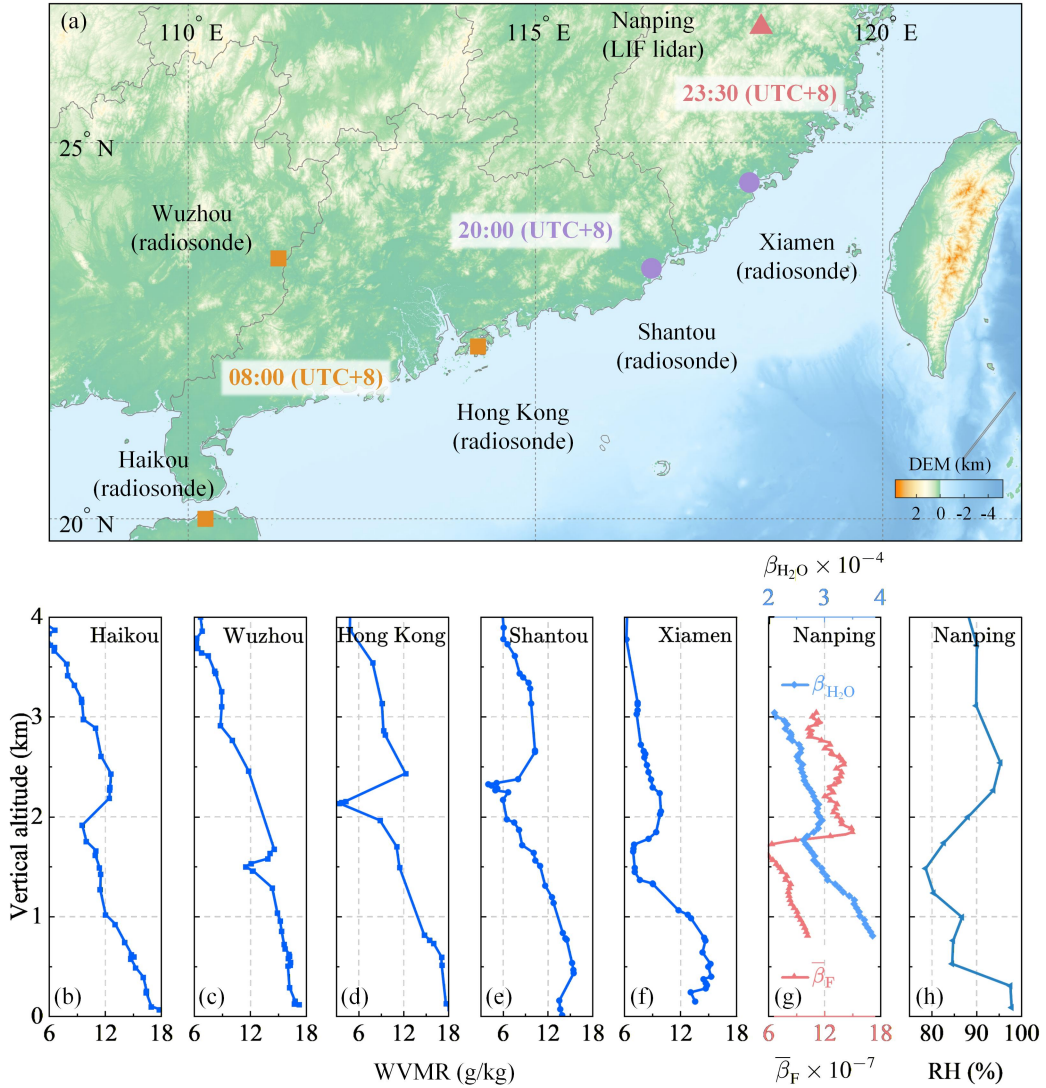


Figure 7. Radiosonde, LIF lidar, and reanalysis profiles for 19 April 2024 (UTC+8), Case 1. (a) Map overview of radiosonde launch sites and the LIF lidar site; marker colors and shapes indicate acquisition time; the LIF lidar measurement period is 19 April 2024, 23:19–20 April 00:05 (UTC+8). (b–f) Water vapor mixing ratio (WVMR) profiles from radiosonde measurements. (g) Water vapor Raman backscatter coefficient $\beta_{\text{H}_2\text{O}} - \beta_{\text{H}_2\text{O}}$ ($\text{Mm}^{-1} - \text{sr}^{-1}$) and spectral fluorescence backscatter coefficient $\bar{\beta}_{\text{F}}$ ($\text{Mm}^{-1} - \text{sr}^{-1} - \text{nm}^{-1}$) profiles. (h) ERA5 RH profile for Nanping at 19 April 2024, 23:00 (UTC+8).

layer. Consistent with the high sensitivity of LIF lidar reported in Europe (Gast et al., 2025; Reichardt et al., 2025), these results
345 show that LIF lidar can detect faint BBA fluorescence signals from relatively weak fires in Asia. Fluorescence spectral analysis
reveals a peak similar to those reported in previous in-situ studies of certain hazardous organics. However, the peak wavelengths
of fluorescence spectra differ from previous LIF lidar studies, suggesting compositional variability linked to source types or
aging processes. Notably, co-transport of water vapor with the BBA was also observed, which may enhance aerosol processing
and increase impacts in downwind regions.

350 March marks the peak of seasonal biomass burning across the ICP, with widespread agricultural burning (for planting
preparation) and forest fires (Gautam et al., 2013; Huang et al., 2016). As South China lies downwind of the ICP, it provides
a favorable setting for long-term LIF lidar observations of transported BBA across different stages of the burning season. To
improve quantitative aerosol classification, a LIF lidar system that integrates elastic scattering, depolarization, and fluorescence
detection is under development. It will enable direct retrieval of spectral fluorescence capacity G_F (Reichardt, 2014) and
355 depolarization ratio—key parameters for refining aerosol type differentiation (Veselovskii et al., 2022b) and gaining deeper
insights into regional BBA characteristics.

Appendix A: Meteorological parameters and cases comparison

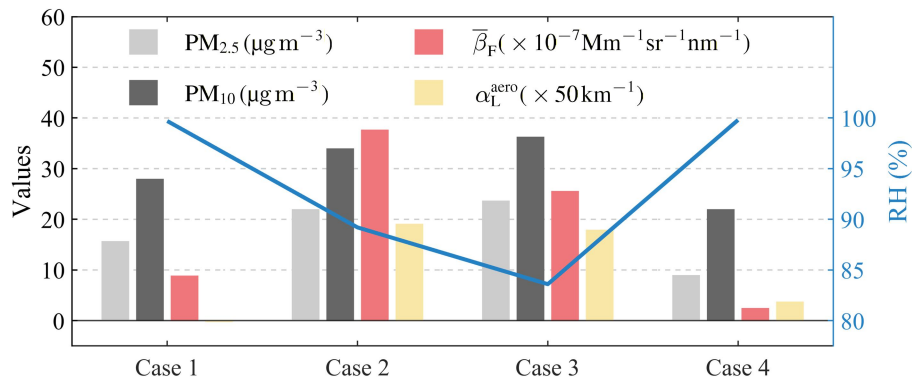


Figure A1. Comparison of key parameters: averaged $\bar{\beta}_F$, α_L^{aero} (0.8–1.4 km), surface RH, and surface PM concentrations. The values of α_L^{aero} have been multiplied by ~~100~~50 for clarity. Note that the averaged α_L^{aero} for Case 1 is negative, which can be attributed to overestimated molecular extinction or retrieval uncertainties associated with temperature and pressure profiles (Ansmann et al., 1992b).

Appendix B: Source attribution of Case 1 with a starting altitude of 1 km

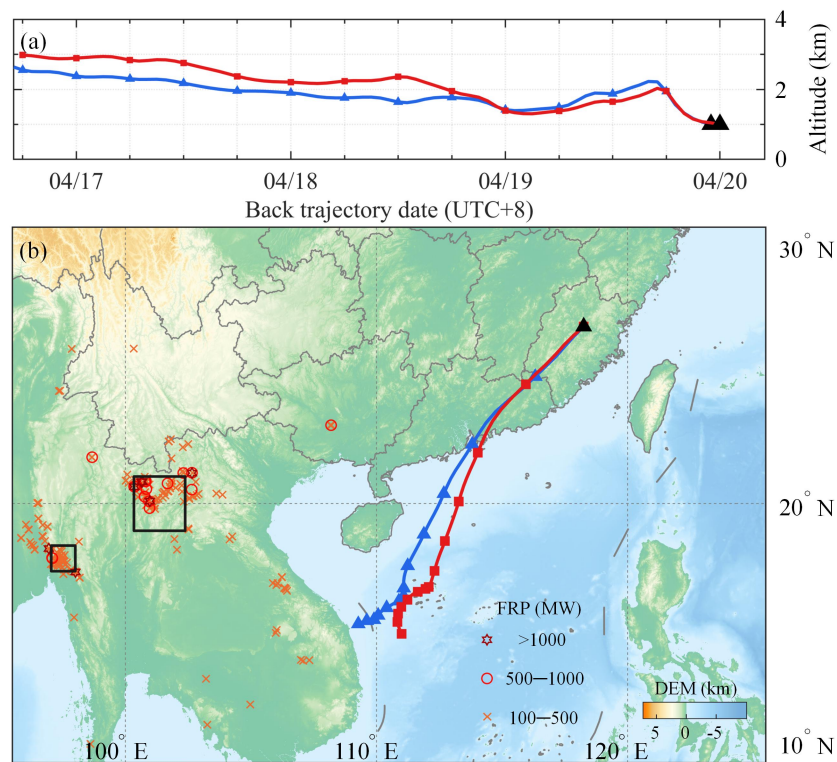


Figure B1. HYSPLIT backward trajectory analysis initialized at 1 km (the LIF lidar site marked by black triangle). (a) Vertical variation of air mass altitude for the study period. (b) Horizontal (longitude-latitude) trajectories overlaid on presumed vegetation fire locations; marker colors and shapes indicate FRP levels.

Appendix C: Fluorescence spectra of previous studies

Table C1. Previous in-situ studies showing fluorescence signatures similar to the BBA spectrum observed in Case 1.

Substances	Excitation/emission wavelength (nm)	References
Pyrene	355/450–470	
Fluoranthene	355/460–480	(Zhang et al., 2019)
BBA (volume correction)	355/450–470	
Cluster 5 (from ambient air)	351/440–470	(Pan et al., 2012)
HULIS	340/475 (max)	(Muller et al., 2008)
Fresh fulvic acids	332–358/410–456	(Klapper et al., 2002)
Fluoranthene	355/450–470	(Louzon et al., 2025)

Table C2. Previously reported LIF lidar fluorescence peaks of BBA.

Origin or time	Excitation/reported peak wavelengths (nm)	References
East and west Canada	355/505–518	
West Canada	355/498–535	(Reichardt et al., 2025)
In gardening season	355/499–540	
American, Siberian	355/513, 560	(Veselovskii et al., 2025)

360 *Data availability.* Lidar data used in this study can be provided for non-commercial research purposes upon request to the first author (zkl@nuist.edu.cn).

Author contributions. ZL: methodology, data curation, formal analysis, visualization, writing (original draft). DT: conceptualization, investigation, writing (review and editing). TW: methodology, writing (review and editing). SY: writing (review and editing). JC: writing (review and editing). KW: writing (review and editing). ZZ: writing (review and editing). JH: writing (review and editing). HH: writing (review and editing). YW: writing (review and editing). HX: resources, supervision, writing (review and editing).

365

Competing interests. The authors declare that they have no conflict of interests.

Acknowledgements. The authors thank the following data sources: the NOAA Air Resources Laboratory (ARL) for providing the HYSPLIT model (<https://www.ready.noaa.gov/>), NASA FIRMS (<https://firms.modaps.eosdis.nasa.gov/>) and NASA worldview (<https://worldview.earthdata.nasa.gov/>) for providing satellite products, NASA and PHOTON for providing AERONET
370 (<https://aeronet.gsfc.nasa.gov/>) sites data (Site managers: Sumaman Buntoung and Somjet Pattarapanitchai), the University of Wyoming's weather website (<https://weather.uwyo.edu/>) for providing radiosonde data, ECMWF for providing ERA5 data (<https://cds.climate.copernicus.eu/>), NASA for providing MERRA-2 data (<https://disc.gsfc.nasa.gov/>), CNEMC for providing air quality data (available at <https://quotsoft.net/air/>), and NOAA (<https://www.ncei.noaa.gov/>) for providing DEM data.

References

- 375 Ansmann, A., Riebesell, M., and Weitkamp, C.: Measurement of atmospheric aerosol extinction profiles with a Raman lidar, *Opt. Lett.*, 15, 746–748, <https://doi.org/10.1364/OL.15.000746>, 1990.
- Ansmann, A., Riebesell, M., Wandinger, U., Weitkamp, C., Voss, E., Lahmann, W., and Michaelis, W.: Combined raman elastic-backscatter LIDAR for vertical profiling of moisture, aerosol extinction, backscatter, and LIDAR ratio, *Applied Physics B*, 55, 18–28, <https://doi.org/10.1007/BF00348608>, 1992a.
- 380 Ansmann, A., Wandinger, U., Riebesell, M., Weitkamp, C., and Michaelis, W.: Independent measurement of extinction and backscatter profiles in cirrus clouds by using a combined Raman elastic-backscatter lidar, *Appl. Opt.*, 31, 7113–7131, <https://doi.org/10.1364/AO.31.007113>, 1992b.
- Ansmann, A., Ohneiser, K., Mamouri, R.-E., Knopf, D. A., Veselovskii, I., Baars, H., Engelmann, R., Foth, A., Jimenez, C., Seifert, P., and Barja, B.: Tropospheric and stratospheric wildfire smoke profiling with lidar: mass, surface area, CCN, and INP retrieval, *Atmospheric Chemistry and Physics*, 21, 9779–9807, <https://doi.org/10.5194/acp-21-9779-2021>, 2021.
- 385 Baumgarten, G.: Doppler Rayleigh/Mie/Raman lidar for wind and temperature measurements in the middle atmosphere up to 80 km, *Atmospheric Measurement Techniques*, 3, 1509–1518, <https://doi.org/10.5194/amt-3-1509-2010>, 2010.
- Chang, S.-S., Lee, W.-J., Wang, L.-C., Lin, N.-H., and Chang-Chien, G.-P.: Influence of the Southeast Asian biomass burnings on the atmospheric persistent organic pollutants observed at near sources and receptor site, *Atmospheric Environment*, 78, 184–194, <https://doi.org/https://doi.org/10.1016/j.atmosenv.2012.07.074>, 2013.
- 390 Chavan, P., Fadnavis, S., Chakroborty, T., Sioris, C. E., Griessbach, S., and Müller, R.: The outflow of Asian biomass burning carbonaceous aerosol into the upper troposphere and lower stratosphere in spring: radiative effects seen in a global model, *Atmospheric Chemistry and Physics*, 21, 14 371–14 384, <https://doi.org/10.5194/acp-21-14371-2021>, 2021.
- Chi, K. H., Lin, C.-Y., Yang, C.-F. O., Wang, J.-L., Lin, N.-H., Sheu, G.-R., and Lee, C.-T.: PCDD/F Measurement at a High-Altitude Station in Central Taiwan: Evaluation of Long-Range Transport of PCDD/Fs during the Southeast Asia Biomass Burning Event, *Environmental Science & Technology*, 44, 2954–2960, <https://doi.org/10.1021/es1000984>, 2010.
- 395 Chouza, F., Leblanc, T., Brewer, M., Wang, P., Martucci, G., Haefele, A., Vèrèmes, H., Duflot, V., Payen, G., and Keckhut, P.: The impact of aerosol fluorescence on long-term water vapor monitoring by Raman lidar and evaluation of a potential correction method, *Atmospheric Measurement Techniques*, 15, 4241–4256, <https://doi.org/10.5194/amt-15-4241-2022>, 2022.
- 400 Christesen, S. D., Wong, A., DeSha, M. S., Mellow, C. N., Wilson, M. W., and Butler, J. C.: Ultraviolet-laser-induced fluorescence of aerosolized bacterial spores, in: *Advances in Fluorescence Sensing Technology*, edited by Lakowicz, J. R. and Thompson, R. B., vol. 1885, pp. 114 – 121, International Society for Optics and Photonics, SPIE, <https://doi.org/10.1117/12.144702>, 1993.
- Dajuma, A., Ogunjobi, K. O., Vogel, H., Knippertz, P., Silué, S., N’Datchoh, E. T., Yoboué, V., and Vogel, B.: Downward cloud venting of the central African biomass burning plume during the West Africa summer monsoon, *Atmospheric Chemistry and Physics*, 20, 5373–5390, <https://doi.org/10.5194/acp-20-5373-2020>, 2020.
- 405 Dang, C., Segal-Rozenhaimer, M., Che, H., Zhang, L., Formenti, P., Taylor, J., Dobracki, A., Purdue, S., Wong, P.-S., Nenes, A., Sedlacek III, A., Coe, H., Redemann, J., Zuidema, P., Howell, S., and Haywood, J.: Biomass burning and marine aerosol processing over the southeast Atlantic Ocean: a TEM single-particle analysis, *Atmospheric Chemistry and Physics*, 22, 9389–9412, <https://doi.org/10.5194/acp-22-9389-2022>, 2022.

- 410 Duschek, F., Fellner, L., Gebert, F., Grünewald, K., Köhntopp, A., Kraus, M., Mahnke, P., Pargmann, C., Tomaso, H., and Walter, A.: Standoff detection and classification of bacteria by multispectral laser-induced fluorescence, *Advanced Optical Technologies*, 6, 75–83, <https://doi.org/doi:10.1515/aot-2016-0066>, 2017.
- Fadnavis, S., Semeniuk, K., Pozzoli, L., Schultz, M. G., Ghude, S. D., Das, S., and Kakatkar, R.: Transport of aerosols into the UTLS and their impact on the Asian monsoon region as seen in a global model simulation, *Atmospheric Chemistry and Physics*, 13, 8771–8786, <https://doi.org/10.5194/acp-13-8771-2013>, 2013.
- 415 Farsund, O., Rustad, G., Kasen, I., and Haavardsholm, T. V.: Required Spectral Resolution for Bioaerosol Detection Algorithms Using Standoff Laser-Induced Fluorescence Measurements, *IEEE Sensors Journal*, 10, 655–661, <https://doi.org/10.1109/JSEN.2009.2037794>, 2010.
- Farsund, Ø., Rustad, G., and Skogan, G.: Standoff detection of biological agents using laser induced fluorescence—a comparison of 294 nm and 355 nm excitation wavelengths, *Biomed. Opt. Express*, 3, 2964–2975, <https://doi.org/10.1364/BOE.3.002964>, 2012.
- 420 Fiedler, J. and Baumgarten, G.: The ALOMAR Rayleigh/Mie/Raman lidar: status after 30 years of operation, *Atmospheric Measurement Techniques*, 17, 5841–5859, <https://doi.org/10.5194/amt-17-5841-2024>, 2024.
- Gast, B., Jimenez, C., Ansmann, A., Haarig, M., Engelmann, R., Fritzsche, F., Floutsi, A. A., Griesche, H., Ohneiser, K., Hofer, J., Radenz, M., Baars, H., Seifert, P., and Wandinger, U.: Invisible aerosol layers: improved lidar detection capabilities by means of laser-induced aerosol fluorescence, *Atmospheric Chemistry and Physics*, 25, 3995–4011, <https://doi.org/10.5194/acp-25-3995-2025>, 2025.
- 425 Gautam, R., Hsu, N. C., Eck, T. F., Holben, B. N., Janjai, S., Jantarach, T., Tsay, S.-C., and Lau, W. K.: Characterization of aerosols over the Indochina peninsula from satellite-surface observations during biomass burning pre-monsoon season, *Atmospheric Environment*, 78, 51–59, <https://doi.org/https://doi.org/10.1016/j.atmosenv.2012.05.038>, 2013.
- Gelaro, R., McCarty, W., Suárez, M. J., Todling, R., Molod, A., Takacs, L., Randles, C. A., Darmenov, A., Bosilovich, M. G., Reichle, R., Wargan, K., Coy, L., Cullather, R., Draper, C., Akella, S., Buchard, V., Conaty, A., da Silva, A. M., Gu, W., Kim, G.-K., Koster, R., Lucchesi, R., Merkova, D., Nielsen, J. E., Partyka, G., Pawson, S., Putman, W., Rienecker, M., Schubert, S. D., Sienkiewicz, M., and Zhao, B.: The Modern-Era Retrospective Analysis for Research and Applications, Version 2 (MERRA-2), *Journal of Climate*, 30, 5419 – 5454, <https://doi.org/10.1175/JCLI-D-16-0758.1>, 2017.
- 430 Wargan, K., Coy, L., Cullather, R., Draper, C., Akella, S., Buchard, V., Conaty, A., da Silva, A. M., Gu, W., Kim, G.-K., Koster, R., Lucchesi, R., Merkova, D., Nielsen, J. E., Partyka, G., Pawson, S., Putman, W., Rienecker, M., Schubert, S. D., Sienkiewicz, M., and Zhao, B.: The Modern-Era Retrospective Analysis for Research and Applications, Version 2 (MERRA-2), *Journal of Climate*, 30, 5419 – 5454, <https://doi.org/10.1175/JCLI-D-16-0758.1>, 2017.
- 435 Gidarakou, M., Papayannis, A., Gao, K., Gidarakos, P., Crouzy, B., Foskinis, R., Erb, S., **Brem, B. T.**, Zhang, C., Lieberherr, G., Collaud Coen, M., Sikoparija, B., Kanji, Z. A., Clot, B., Calpini, B., Giagka, E., and Nenes, A.: Profiling pollen and biomass burning particles over Payerne, Switzerland using laser-induced fluorescence lidar and *in-situ* *in situ* techniques during the 2023 PERICLES campaign, *EGUsphere, 2025, 1–34, , 2025*. *Atmospheric Chemistry and Physics*, 26, 923–945, <https://doi.org/10.5194/acp-26-923-2026>, 2026.
- Giglio, L., Schroeder, W., and Justice, C. O.: The collection 6 MODIS active fire detection algorithm and fire products, *Remote Sensing of Environment*, 178, 31–41, <https://doi.org/https://doi.org/10.1016/j.rse.2016.02.054>, 2016.
- 440 Haarig, M., Engelmann, R., Baars, H., Gast, B., Althausen, D., and Ansmann, A.: Discussion of the spectral slope of the lidar ratio between 355 and 1064 nm from multiwavelength Raman lidar observations, *Atmospheric Chemistry and Physics*, 25, 7741–7763, <https://doi.org/10.5194/acp-25-7741-2025>, 2025.
- Heese, B., Baars, H., Bohlmann, S., Althausen, D., and Deng, R.: Continuous vertical aerosol profiling with a multi-wavelength Raman polarization lidar over the Pearl River Delta, China, *Atmospheric Chemistry and Physics*, 17, 6679–6691, <https://doi.org/10.5194/acp-17-6679-2017>, 2017.
- 445

- Hersbach, H., Bell, B., Berrisford, P., Hirahara, S., Horányi, A., Muñoz-Sabater, J., Nicolas, J., Peubey, C., Radu, R., Schepers, D., Simmons, A., Soci, C., Abdalla, S., Abellan, X., Balsamo, G., Bechtold, P., Biavati, G., Bidlot, J., Bonavita, M., De Chiara, G., Dahlgren, P., Dee, D., Diamantakis, M., Dragani, R., Flemming, J., Forbes, R., Fuentes, M., Geer, A., Haimberger, L., Healy, S., Hogan, R. J., Hólm, E., Janisková, M., Keeley, S., Laloyaux, P., Lopez, P., Lupu, C., Radnoti, G., de Rosnay, P., Rozum, I., Vamborg, F., Villaume, S., and Thépaut, J.-N.: The ERA5 global reanalysis, *Quarterly Journal of the Royal Meteorological Society*, 146, 1999–2049, <https://doi.org/https://doi.org/10.1002/qj.3803>, 2020.
- Hodshire, A. L., Akherati, A., Alvarado, M. J., Brown-Steiner, B., Jathar, S. H., Jimenez, J. L., Kreidenweis, S. M., Lonsdale, C. R., Onasch, T. B., Ortega, A. M., and Pierce, J. R.: Aging Effects on Biomass Burning Aerosol Mass and Composition: A Critical Review of Field and Laboratory Studies, *Environmental Science & Technology*, 53, 10007–10022, <https://doi.org/10.1021/acs.est.9b02588>, 2019.
- Holben, B., Eck, T., Slutsker, I., Tanré, D., Buis, J., Setzer, A., Vermote, E., Reagan, J., Kaufman, Y., Nakajima, T., Lavenu, F., Jankowiak, I., and Smirnov, A.: AERONET—A Federated Instrument Network and Data Archive for Aerosol Characterization, Remote Sensing of Environment, 66, 1–16, [https://doi.org/https://doi.org/10.1016/S0034-4257\(98\)00031-5](https://doi.org/https://doi.org/10.1016/S0034-4257(98)00031-5), 1998.
- Hu, Q., Goloub, P., Veselovskii, I., and Podvin, T.: The characterization of long-range transported North American biomass burning plumes: what can a multi-wavelength Mie–Raman-polarization-fluorescence lidar provide?, *Atmospheric Chemistry and Physics*, 22, 5399–5414, <https://doi.org/10.5194/acp-22-5399-2022>, 2022.
- Hu, Q., Goloub, P., Veselovskii, I., Podvin, T., Dubois, G., Khaykin, S., Boissière, W., Ducos, F., and Korenskiy, M.: Advanced insights into biomass burning aerosols during the 2023 Canadian wildfires from dual-site Raman and fluorescence lidar observations, *EGUsphere*, 2025, 1–40, <https://doi.org/10.5194/egusphere-2025-5041>, 2025.
- Huang, W.-R., Wang, S.-H., Yen, M.-C., Lin, N.-H., and Promchote, P.: Interannual variation of springtime biomass burning in Indochina: Regional differences, associated atmospheric dynamical changes, and downwind impacts, *Journal of Geophysical Research: Atmospheres*, 121, 10,016–10,028, <https://doi.org/https://doi.org/10.1002/2016JD025286>, 2016.
- Huang, X., Ding, K., Liu, J., Wang, Z., Tang, R., Xue, L., Wang, H., Zhang, Q., Tan, Z.-M., Fu, C., Davis, S. J., Andreae, M. O., and Ding, A.: Smoke-weather interaction affects extreme wildfires in diverse coastal regions, *Science*, 379, 457–461, <https://doi.org/10.1126/science.add9843>, 2023.
- Huang, Z., Wang, Y., Zhou, T., Ji, Y., Bi, J., Shi, J., Wen, H., and Huang, J.: Raman-Polarization-Fluorescence Spectroscopic Lidar for Real-Time Detection of Humic-like Substance Profiles, *Environmental Science & Technology*, 59, 7235–7245, <https://doi.org/10.1021/acs.est.5c00028>, 2025.
- Immler, F., Engelbart, D., and Schrems, O.: Fluorescence from atmospheric aerosol detected by a lidar indicates biogenic particles in the lowermost stratosphere, *Atmospheric Chemistry and Physics*, 5, 345–355, <https://doi.org/10.5194/acp-5-345-2005>, 2005.
- Jiang, Y., Yang, H., Tan, W., Chen, S., Chen, H., Guo, P., Xu, Q., Gong, J., and Yu, Y.: Observation and Classification of Low-Altitude Haze Aerosols Using Fluorescence–Raman–Mie Polarization Lidar in Beijing during Spring 2024, *Remote Sensing*, 16, <https://doi.org/10.3390/rs16173225>, 2024.
- Kim, S.-W., Chazette, P., Dulac, F., Sanak, J., Johnson, B., and Yoon, S.-C.: Vertical structure of aerosols and water vapor over West Africa during the African monsoon dry season, *Atmospheric Chemistry and Physics*, 9, 8017–8038, <https://doi.org/10.5194/acp-9-8017-2009>, 2009.
- Klapper, L., McKnight, D. M., Fulton, J. R., Blunt-Harris, E. L., Nevin, K. P., Lovley, D. R., and Hatcher, P. G.: Fulvic Acid Oxidation State Detection Using Fluorescence Spectroscopy, *Environmental Science & Technology*, 36, 3170–3175, <https://doi.org/10.1021/es0109702>, 2002.

- 485 Leifer, I., Lehr, W. J., Simecek-Beatty, D., Bradley, E., Clark, R., Dennison, P., Hu, Y., Matheson, S., Jones, C. E., Holt, B., Reif, M., Roberts, D. A., Svejksky, J., Swayze, G., and Wozencraft, J.: State of the art satellite and airborne marine oil spill remote sensing: Application to the BP Deepwater Horizon oil spill, *Remote Sensing of Environment*, 124, 185–209, <https://doi.org/https://doi.org/10.1016/j.rse.2012.03.024>, 2012.
- Li, B., Chen, S., Zhang, Y., Chen, H., and Guo, P.: Fluorescent aerosol observation in the lower atmosphere with
490 an integrated fluorescence-Mie lidar, *Journal of Quantitative Spectroscopy and Radiative Transfer*, 227, 211–218, <https://doi.org/https://doi.org/10.1016/j.jqsrt.2019.02.019>, 2019.
- Lin, N.-H., Tsay, S.-C., Maring, H. B., Yen, M.-C., Sheu, G.-R., Wang, S.-H., Chi, K. H., Chuang, M.-T., Ou-Yang, C.-F., Fu, J. S., Reid, J. S., Lee, C.-T., Wang, L.-C., Wang, J.-L., Hsu, C. N., Sayer, A. M., Holben, B. N., Chu, Y.-C., Nguyen, X. A., Sopajaree, K., Chen, S.-J., Cheng, M.-T., Tsuang, B.-J., Tsai, C.-J., Peng, C.-M., Schnell, R. C., Conway, T., Chang, C.-T., Lin, K.-S., Tsai, Y. I., Lee, W.-J.,
495 Chang, S.-C., Liu, J.-J., Chiang, W.-L., Huang, S.-J., Lin, T.-H., and Liu, G.-R.: An overview of regional experiments on biomass burning aerosols and related pollutants in Southeast Asia: From BASE-ASIA and the Dongsha Experiment to 7-SEAS, *Atmospheric Environment*, 78, 1–19, <https://doi.org/https://doi.org/10.1016/j.atmosenv.2013.04.066>, 2013.
- Lin, N.-H., Sayer, A. M., Wang, S.-H., Loftus, A. M., Hsiao, T.-C., Sheu, G.-R., Hsu, N. C., Tsay, S.-C., and Chantara, S.: Interactions between biomass-burning aerosols and clouds over Southeast Asia: Current status, challenges, and perspectives, *Environmental Pollution*,
500 195, 292–307, <https://doi.org/https://doi.org/10.1016/j.envpol.2014.06.036>, 2014.
- Liu, F., Yi, F., He, Y., Yin, Z., Zhang, Y., and Yu, C.: Spectrally Resolved Raman Lidar to Measure Backscatter Spectra of Atmospheric Three-Phase Water and Fluorescent Aerosols Simultaneously: Instrument, Methodology, and Preliminary Results, *IEEE Transactions on Geoscience and Remote Sensing*, 60, 1–13, <https://doi.org/10.1109/TGRS.2022.3166191>, 2022.
- Liu, L., Mao, Y.-H., and Liao, H.: The impact of biomass burning emissions in Southeast Asia on black carbon aerosols in southern China, *Atmospheric Environment*, 358, 121–135, <https://doi.org/https://doi.org/10.1016/j.atmosenv.2025.121352>, 2025.
- Louzon, M., Bertoncini, T., Casañas, N., Perrette, Y., Plassart, G., Quiers, M., Wallet, T., Kamel, M., and Aleya, L.: Laser-Induced Solid-Phase UV Fluorescence Spectroscopy for Rapid Detection of Polycyclic Aromatic Hydrocarbons in the Land Snail Bioindicator, *Cantareus aspersus*, *Biosensors*, 15, <https://doi.org/10.3390/bios15070450>, 2025.
- 510 Majdi, M., Turquety, S., Sartelet, K., Legorgne, C., Menut, L., and Kim, Y.: Impact of wildfires on particulate matter in the Euro-Mediterranean in 2007: sensitivity to some parameterizations of emissions in air quality models, *Atmospheric Chemistry and Physics*, 19, 785–812, <https://doi.org/10.5194/acp-19-785-2019>, 2019.
- Mattis, I., Ansmann, A., Althausen, D., Jaenisch, V., Wandinger, U., Müller, D., Arshinov, Y. F., Bobrovnikov, S. M., and Serikov, I. B.: Relative-humidity profiling in the troposphere with a Raman lidar, *Appl. Opt.*, 41, 6451–6462, <https://doi.org/10.1364/AO.41.006451>,
515 2002.
- Meggers, W. F. and Kiess, C. C.: False Spectra from Diffraction Gratings Part I. Secondary Spectra, *J. Opt. Soc. Am.*, 6, 417–429, <https://doi.org/10.1364/JOSA.6.000417>, 1922.
- Muller, C. L., Baker, A., Hutchinson, R., Fairchild, I. J., and Kidd, C.: Analysis of rainwater dissolved organic carbon compounds using fluorescence spectrophotometry, *Atmospheric Environment*, 42, 8036–8045, <https://doi.org/https://doi.org/10.1016/j.atmosenv.2008.06.042>,
520 2008.

- Nguyen, L. S. P., Huang, H.-Y., Lei, T. L., Bui, T. T., Wang, S.-H., Chi, K. H., Sheu, G.-R., Lee, C.-T., Ou-Yang, C.-F., and Lin, N.-H.: Characterizing a landmark biomass-burning event and its implication for aging processes during long-range transport, *Atmospheric Environment*, 241, 117 766, <https://doi.org/https://doi.org/10.1016/j.atmosenv.2020.117766>, 2020.
- 525 Pan, Y.-L.: Detection and characterization of biological and other organic-carbon aerosol particles in atmosphere using fluorescence, *Journal of Quantitative Spectroscopy and Radiative Transfer*, 150, 12–35, <https://doi.org/https://doi.org/10.1016/j.jqsrt.2014.06.007>, 2015.
- Pan, Y.-L., Huang, H., and Chang, R. K.: Clustered and integrated fluorescence spectra from single atmospheric aerosol particles excited by a 263- and 351-nm laser at New Haven, CT, and Adelphi, MD, *Journal of Quantitative Spectroscopy and Radiative Transfer*, 113, 2213–2221, <https://doi.org/https://doi.org/10.1016/j.jqsrt.2012.07.028>, 2012.
- 530 Pistone, K., Zuidema, P., Wood, R., Diamond, M., da Silva, A. M., Ferrada, G., Saide, P. E., Ueyama, R., Ryoo, J.-M., Pfister, L., Podolske, J., Noone, D., Bennett, R., Stith, E., Carmichael, G., Redemann, J., Flynn, C., LeBlanc, S., Segal-Rozenhaimer, M., and Shinozuka, Y.: Exploring the elevated water vapor signal associated with the free tropospheric biomass burning plume over the southeast Atlantic Ocean, *Atmospheric Chemistry and Physics*, 21, 9643–9668, <https://doi.org/10.5194/acp-21-9643-2021>, 2021.
- Pistone, K., Wilcox, E. M., Zuidema, P., Giordano, M., Podolske, J., LeBlanc, S. E., Kacenelenbogen, M., Howell, S. G., and Freitag, S.: Vertical structure of a springtime smoky and humid troposphere over the southeast Atlantic from aircraft and reanalysis, *Atmospheric Chemistry and Physics*, 24, 7983–8005, <https://doi.org/10.5194/acp-24-7983-2024>, 2024.
- 535 Platt, U., Pfeilsticker, K., and Vollmer, M.: *Radiation and Optics in the Atmosphere*, pp. 1475–1517, Springer Berlin Heidelberg, Berlin, Heidelberg, ISBN 978-3-642-19409-2, https://doi.org/10.1007/978-3-642-19409-2_23, 2012.
- Pöhlker, C., Huffman, J. A., and Pöschl, U.: Autofluorescence of atmospheric bioaerosols – fluorescent biomolecules and potential interferences, *Atmospheric Measurement Techniques*, 5, 37–71, <https://doi.org/10.5194/amt-5-37-2012>, 2012.
- 540 Qin, Y., Wang, H., Wang, Y., Lu, X., Tang, H., Zhang, J., Li, L., and Fan, S.: Wildfires in Southeast Asia pollute the atmosphere in the northern South China Sea, *Science Bulletin*, 69, 1011–1015, <https://doi.org/https://doi.org/10.1016/j.scib.2024.02.026>, 2024.
- Rao, Z., He, T., Hua, D., Wang, Y., Wang, X., Chen, Y., and Le, J.: Preliminary measurements of fluorescent aerosol number concentrations using a laser-induced fluorescence lidar, *Appl. Opt.*, 57, 7211–7215, <https://doi.org/10.1364/AO.57.007211>, 2018.
- Reichardt, J.: Cloud and Aerosol Spectroscopy with Raman Lidar, *Journal of Atmospheric and Oceanic Technology*, 31, 1946 – 1963, <https://doi.org/10.1175/JTECH-D-13-00188.1>, 2014.
- 545 Reichardt, J., Wandinger, U., Klein, V., Mattis, I., Hilber, B., and Begbie, R.: RAMSES: German Meteorological Service autonomous Raman lidar for water vapor, temperature, aerosol, and cloud measurements, *Appl. Opt.*, 51, 8111–8131, <https://doi.org/10.1364/AO.51.008111>, 2012.
- Reichardt, J., Behrendt, O., and Laueremann, F.: Spectrometric fluorescence and Raman lidar: absolute calibration of aerosol fluorescence spectra and fluorescence correction of humidity measurements, *Atmospheric Measurement Techniques*, 16, 1–13, <https://doi.org/10.5194/amt-16-1-2023>, 2023.
- 550 Reichardt, J., Laueremann, F., and Behrendt, O.: Fluorescence spectra of atmospheric aerosols, *Atmospheric Chemistry and Physics*, 25, 5857–5892, <https://doi.org/10.5194/acp-25-5857-2025>, 2025.
- Reichardt, Jens, Leinweber, Ronny, and Schwebe, Anne: Fluorescing aerosols and clouds: investigations of co-existence, *EPJ Web Conf.*, 176, 05 010, <https://doi.org/10.1051/epjconf/201817605010>, 2018.
- 555 Richardson, S., Mytilinaios, M., Foskinis, R., Kyrou, C., Papayannis, A., Pyrri, I., Giannoutsou, E., and Adamakis, I.: Bioaerosol detection over Athens, Greece using the laser induced fluorescence technique, *Science of The Total Environment*, 696, 133 906, <https://doi.org/https://doi.org/10.1016/j.scitotenv.2019.133906>, 2019.

- Rubin, J. I., Reid, J. S., Xian, P., Selman, C. M., and Eck, T. F.: A global evaluation of daily to seasonal aerosol and water vapor relationships using a combination of AERONET and NAAPS reanalysis data, *Atmospheric Chemistry and Physics*, 23, 4059–4090, <https://doi.org/10.5194/acp-23-4059-2023>, 2023.
- Saito, Y., Kakuda, K., Yokoyama, M., Kubota, T., Tomida, T., and Park, H.-D.: Design and daytime performance of laser-induced fluorescence spectrum lidar for simultaneous detection of multiple components, dissolved organic matter, phycoerythrin, and chlorophyll in river water, *Appl. Opt.*, 55, 6727–6734, <https://doi.org/10.1364/AO.55.006727>, 2016.
- Saito, Y., Ichihara, K., Morishita, K., Uchiyama, K., Kobayashi, F., and Tomida, T.: Remote Detection of the Fluorescence Spectrum of Natural Pollens Floating in the Atmosphere Using a Laser-Induced-Fluorescence Spectrum (LIFS) Lidar, *Remote Sensing*, 10, <https://doi.org/10.3390/rs10101533>, 2018.
- Shan, X., Xu, J., Li, Y., Han, F., Du, X., Mao, J., Chen, Y., He, Y., Meng, F., and Dai, X.: Analysis of the origin of peak aerosol optical depth in springtime over the Gulf of Tonkin, *Journal of Environmental Sciences*, 40, 129–137, <https://doi.org/https://doi.org/10.1016/j.jes.2015.10.026>, 2016.
- ~~Shang, X., Xia, H., Dou, X., Shangguan, M., Li, M., and Wang, C.: Adaptive inversion algorithm for 1.5 μ m visibility lidar incorporating in situ Angstrom wavelength exponent, *Optics Communications*, 418, 129–134, 2018.~~
- Shangguan, M., Guo, Y., Liao, Z., and Lee, Z.: Sensing profiles of the volume scattering function at 180° using a single-photon oceanic fluorescence lidar, *Opt. Express*, 31, 40393–40410, <https://doi.org/10.1364/OE.505615>, 2023a.
- Shangguan, M., Yang, Z., Shangguan, M., Lin, Z., Liao, Z., Guo, Y., and Liu, C.: Remote sensing oil in water with an all-fiber underwater single-photon Raman lidar, *Appl. Opt.*, 62, 5301–5305, <https://doi.org/10.1364/AO.488872>, 2023b.
- Shangguan, M., Guo, Y., and Liao, Z.: Shipborne single-photon fluorescence oceanic lidar: instrumentation and inversion, *Opt. Express*, 32, 10204–10218, <https://doi.org/10.1364/OE.515477>, 2024.
- Shi, S., Cheng, T., Gu, X., Guo, H., Wu, Y., and Wang, Y.: Biomass burning aerosol characteristics for different vegetation types in different aging periods, *Environment International*, 126, 504–511, <https://doi.org/https://doi.org/10.1016/j.envint.2019.02.073>, 2019.
- Shi, Y. and Yamaguchi, Y.: A high-resolution and multi-year emissions inventory for biomass burning in Southeast Asia during 2001–2010, *Atmospheric Environment*, 98, 8–16, <https://doi.org/https://doi.org/10.1016/j.atmosenv.2014.08.050>, 2014.
- Shoshanim, O.: Detection of bioaerosols using hyperspectral LIF-LIDAR during S/K challenge II campaign at Dugway, *Atmospheric Pollution Research*, 14, 101723, <https://doi.org/https://doi.org/10.1016/j.apr.2023.101723>, 2023.
- Simard, J.-R., Roy, G., Mathieu, P., Larochelle, V., McFee, J., and Ho, J.: Standoff sensing of bioaerosols using intensified range-gated spectral analysis of laser-induced fluorescence, *IEEE Transactions on Geoscience and Remote Sensing*, 42, 865–874, <https://doi.org/10.1109/TGRS.2003.823285>, 2004.
- Stein, A. F., Draxler, R. R., Rolph, G. D., Stunder, B. J. B., Cohen, M. D., and Ngan, F.: NOAA’s HYSPLIT Atmospheric Transport and Dispersion Modeling System, *Bulletin of the American Meteorological Society*, 96, 2059 – 2077, <https://doi.org/10.1175/BAMS-D-14-00110.1>, 2015.
- Sugimoto, N., Huang, Z., Nishizawa, T., Matsui, I., and Tatarov, B.: Fluorescence from atmospheric aerosols observed with a multi-channel lidar spectrometer, *Opt. Express*, 20, 20800–20807, <https://doi.org/10.1364/OE.20.020800>, 2012.
- Sun, L., Zhang, Y., Ouyang, C., Yin, S., Ren, X., and Fu, S.: A portable UAV-based laser-induced fluorescence lidar system for oil pollution and aquatic environment monitoring, *Optics Communications*, 527, 128914, <https://doi.org/https://doi.org/10.1016/j.optcom.2022.128914>, 2023.

- Tang, D., Wei, T., Yuan, J., Xia, H., and Dou, X.: Observation of bioaerosol transport using wideband integrated bioaerosol sensor and coherent Doppler lidar, *Atmospheric Measurement Techniques*, 15, 2819–2838, <https://doi.org/10.5194/amt-15-2819-2022>, 2022.
- Tang, D., Li, Z., and Xia, H.: Clustering of weak fluorescence spectra from bioaerosol in air using laser-induced fluorescence lidar, *Opt. Express*, 33, 24 396–24 412, <https://doi.org/10.1364/OE.560805>, 2025a.
- 600 Tang, R., Zhang, R., Ma, J., Song, K., Go, B. R., Cuevas, R. A. I., Zhou, L., Liang, Z., Vogel, A. L., Guo, S., and Chan, C. K.: Sulfate Formation by Photosensitization in Mixed Incense Burning–Sodium Chloride Particles: Effects of RH, Light Intensity, and Aerosol Aging, *Environmental Science & Technology*, 57, 10 295–10 307, <https://doi.org/10.1021/acs.est.3c02225>, 2023.
- Tang, R., Ma, J., Zhang, R., Cui, W., Qin, Y., Chu, Y., Qin, Y., Vogel, A. L., and Chan, C. K.: Enhanced sulfate formation in mixed biomass burning and sea-salt interactions mediated by photosensitization: effects of chloride, nitrogen-containing compounds, and atmospheric aging, *Atmospheric Chemistry and Physics*, 25, 425–439, <https://doi.org/10.5194/acp-25-425-2025>, 2025b.
- 605 Vasilakopoulou, C. N., Matrali, A., Skyllakou, K., Georgopoulou, M., Aktypis, A., Florou, K., Kaltsonoudis, C., Siouti, E., Kostenidou, E., Błaziak, A., Nenes, A., Papagiannis, S., Eleftheriadis, K., Patoulias, D., Kioutsioukis, I., and Pandis, S. N.: Rapid transformation of wildfire emissions to harmful background aerosol, *npj Climate and Atmospheric Science*, 6, 218, <https://doi.org/10.1038/s41612-023-00544-7>, 2023.
- 610 Venable, D. D., Whiteman, D. N., Calhoun, M. N., Dirisu, A. O., Connell, R. M., and Landulfo, E.: Lamp mapping technique for independent determination of the water vapor mixing ratio calibration factor for a Raman lidar system, *Appl. Opt.*, 50, 4622–4632, <https://doi.org/10.1364/AO.50.004622>, 2011.
- Veselovskii, I., Hu, Q., Goloub, P., Podvin, T., Korenskiy, M., Pujol, O., Dubovik, O., and Lopatin, A.: Combined use of Mie–Raman and fluorescence lidar observations for improving aerosol characterization: feasibility experiment, *Atmospheric Measurement Techniques*, 13, 6691–6701, <https://doi.org/10.5194/amt-13-6691-2020>, 2020.
- 615 Veselovskii, I., Hu, Q., Goloub, P., Podvin, T., Choël, M., Visez, N., and Korenskiy, M.: Mie–Raman–fluorescence lidar observations of aerosols during pollen season in the north of France, *Atmospheric Measurement Techniques*, 14, 4773–4786, <https://doi.org/10.5194/amt-14-4773-2021>, 2021.
- Veselovskii, I., Hu, Q., Ansmann, A., Goloub, P., Podvin, T., and Korenskiy, M.: Fluorescence lidar observations of wildfire smoke inside cirrus: a contribution to smoke–cirrus interaction research, *Atmospheric Chemistry and Physics*, 22, 5209–5221, <https://doi.org/10.5194/acp-22-5209-2022>, 2022a.
- 620 Veselovskii, I., Hu, Q., Goloub, P., Podvin, T., Barchunov, B., and Korenskiy, M.: Combining Mie–Raman and fluorescence observations: a step forward in aerosol classification with lidar technology, *Atmospheric Measurement Techniques*, 15, 4881–4900, <https://doi.org/10.5194/amt-15-4881-2022>, 2022b.
- 625 Veselovskii, I., Kasianik, N., Korenskiy, M., Hu, Q., Goloub, P., Podvin, T., and Liu, D.: Multiwavelength fluorescence lidar observations of smoke plumes, *Atmospheric Measurement Techniques*, 16, 2055–2065, <https://doi.org/10.5194/amt-16-2055-2023>, 2023.
- Veselovskii, I., Hu, Q., Goloub, P., Podvin, T., Boissiere, W., Korenskiy, M., Kasianik, N., Khaykyn, S., and Miri, R.: Derivation of depolarization ratios of aerosol fluorescence and water vapor Raman backscatters from lidar measurements, *Atmospheric Measurement Techniques*, 17, 1023–1036, <https://doi.org/10.5194/amt-17-1023-2024>, 2024.
- 630 Veselovskii, I., Korenskiy, M., Kasianik, N., Barchunov, B., Hu, Q., Goloub, P., and Podvin, T.: Fluorescence properties of long-range-transported smoke: insights from five-channel lidar observations over Moscow during the 2023 wildfire season, *Atmospheric Chemistry and Physics*, 25, 1603–1615, <https://doi.org/10.5194/acp-25-1603-2025>, 2025.

- 635 Wang, Y., Hu, M., Lin, P., Tan, T., Li, M., Xu, N., Zheng, J., Du, Z., Qin, Y., Wu, Y., Lu, S., Song, Y., Wu, Z., Guo, S., Zeng, L., Huang, X., and He, L.: Enhancement in Particulate Organic Nitrogen and Light Absorption of Humic-Like Substances over Tibetan Plateau Due to Long-Range Transported Biomass Burning Emissions, *Environmental Science & Technology*, 53, 14 222–14 232, <https://doi.org/10.1021/acs.est.9b06152>, 2019.
- Wang, Y., Huang, Z., Zhou, T., Bi, J., and Shi, J.: Identification of fluorescent aerosol observed by a spectroscopic lidar over northwest China, *Opt. Express*, 31, 22 157–22 169, <https://doi.org/10.1364/OE.493557>, 2023.
- 640 Wojtanowski, J., Zygmunt, M., Muzal, M., Knysak, P., Młodzianko, A., Gawlikowski, A., Drozd, T., Kopczyński, K., Mierczyk, Z., Kaszczuk, M., Traczyk, M., Gietka, A., Piotrowski, W., Jakubaszek, M., and Ostrowski, R.: Performance verification of a LIF-LIDAR technique for stand-off detection and classification of biological agents, *Optics & Laser Technology*, 67, 25–32, <https://doi.org/https://doi.org/10.1016/j.optlastec.2014.08.013>, 2015.
- Xue, L., Ding, K., Huang, X., Zhu, A., Lou, S., Wang, Z., Xie, Y., and Ding, A.: Biomass Burning Plumes From Indochina Toward Southern China: Predominant Synoptic Weather Processes and Interactions, *Journal of Geophysical Research: Atmospheres*, 130, e2024JD041 813, 645 <https://doi.org/https://doi.org/10.1029/2024JD041813>, 2025.
- Yadav, I. C., Linthoingambi Devi, N., Li, J., Syed, J. H., Zhang, G., and Watanabe, H.: Biomass burning in Indo-China peninsula and its impacts on regional air quality and global climate change-a review, *Environmental Pollution*, 227, 414–427, <https://doi.org/https://doi.org/10.1016/j.envpol.2017.04.085>, 2017.
- Yin, S.: Biomass burning spatiotemporal variations over South and Southeast Asia, *Environment International*, 145, 106 153, 650 <https://doi.org/https://doi.org/10.1016/j.envint.2020.106153>, 2020.
- Yue, S., Li, L., Xu, W., Zhao, J., Ren, H., Ji, D., Li, P., Zhang, Q., Wei, L., Xie, Q., Pan, X., Wang, Z., Sun, Y., and Fu, P.: Biological and Nonbiological Sources of Fluorescent Aerosol Particles in the Urban Atmosphere, *Environmental Science & Technology*, 56, 7588–7597, <https://doi.org/10.1021/acs.est.1c07966>, 2022.
- Yufeng, W., Xueqiao, X., Wei, C., Huige, D., Jingjing, L., and Dengxin, H.: Lidar-based investigation of aerosol hygroscopic growth characteristics using fluorescence capacity, *Opt. Express*, 33, 48 560–48 574, <https://doi.org/10.1364/OE.578064>, 2025.
- Zhang, M., Klimach, T., Ma, N., Könemann, T., Pöhlker, C., Wang, Z., Kuhn, U., Scheck, N., Pöschl, U., Su, H., and Cheng, Y.: Size-Resolved Single-Particle Fluorescence Spectrometer for Real-Time Analysis of Bioaerosols: Laboratory Evaluation and Atmospheric Measurements, *Environmental Science & Technology*, 53, 13 257–13 264, <https://doi.org/10.1021/acs.est.9b01862>, 2019.
- 660 Zhang, Y., Sun, Z., Chen, S., Chen, H., Guo, P., Chen, S., He, J., Wang, J., and Nian, X.: Classification and source analysis of low-altitude aerosols in Beijing using fluorescence–Mie polarization lidar, *Optics Communications*, 479, 126417, <https://doi.org/https://doi.org/10.1016/j.optcom.2020.126417>, 2021.
- Zhao, H., Zhou, Y., Wu, H., Kutser, T., Han, Y., Ma, R., Yao, Z., Zhao, H., Xu, P., Jiang, C., Gu, Q., Ma, S., Wu, L., Chen, Y., Sheng, H., Wan, X., Chen, W., Chen, X., Bai, J., Wu, L., Liu, Q., Sun, W., Yang, S., Hu, M., Liu, C., and Liu, D.: Potential of Mie–Fluorescence–Raman Lidar to Profile Chlorophyll a Concentration in Inland Waters, *Environmental Science & Technology*, 57, 665 14 226–14 236, <https://doi.org/10.1021/acs.est.3c04212>, PMID: 37713595, 2023.
- Zhou, R., Di, D., Li, J., and Li, Z.: Enhanced Moisture Retrieval Near Boundary Layer From Satellite Sounder Data Through Atmospheric–Surface Radiance Separation, *Geophysical Research Letters*, 52, e2024GL113 404, <https://doi.org/https://doi.org/10.1029/2024GL113404>, 2025.

Zhou, S., Collier, S., Jaffe, D. A., Briggs, N. L., Hee, J., Sedlacek III, A. J., Kleinman, L., Onasch, T. B., and Zhang, Q.: Regional influence
670 of wildfires on aerosol chemistry in the western US and insights into atmospheric aging of biomass burning organic aerosol, *Atmospheric
Chemistry and Physics*, 17, 2477–2493, <https://doi.org/10.5194/acp-17-2477-2017>, 2017.